

10-30 μm MAPS OF THE CENTRAL 5 PARSECS OF THE GALAXY:
HEATING OF THE CAVITY AND NEUTRAL-GAS DISK

C. M. Telesco^{1,2}

Space Science Laboratory, ES84

NASA Marshall Space Flight Center, Huntsville, AL 35812

J. A. Davidson¹

SETI Institute, NASA Ames Research Center

MS 245-6, Moffett Field, CA 94035

M. W. Werner¹

Jet Propulsion Laboratory, MS 233-303

4800 Oak Grove Drive, Pasadena, CA 91109

Received — — . — . — . —

¹ Guest Investigator at the Infrared Telescope Facility which is operated by the University of Hawaii under contract to the National Aeronautics and Space Administration,

² Current Address: University of Florida, Department of Astronomy,
SSRB211, Gainesville, FL 32611

ABSTRACT

We present 10, 20, and 30 μm maps of the central $60'' \times 90''$ (RA \times Dec) of the Galaxy made at $4''$ resolution with the MSFC bolometer array. The maps span $2.5 \times 3.8 \text{ pc}$ centered near Sgr A IRS 1 and are the first to show the thermal emission from dust particles in both the ionized cavity and the neutral-gas ring with high sensitivity and an angular resolution as good as several arcsec. The central $40''$ of the emission maps is dominated by radiation from warm dust associated with previously identified filaments. These maps also show for the first time the detailed distribution of dust along the entire Western Arc which is especially prominent at 30 μm . The map of optical depth of 30 μm -emitting dust shows clearly the low-density cavity and the neutral gas ring. For canonical gas-to-dust ratios, the average proton density in the cavity is $\sim 300 \text{ cm}^{-3}$ away from the ionized filaments, with densities in the ring ranging from about $5 \times 10^3 \text{ cm}^{-3}$ in the northwest to about $5 \times 10^4 \text{ cm}^{-3}$ at the densest concentration in the southwest lobe. A prominent tongue of high 30 μm optical depth extends from the northern part of the ring into the cavity near IRS 1, nearly bisecting the cavity; since we detect warm dust in this 30 μm -emitting feature, which we call the Northern Intruder, it must be heated by radiation emitted in the cavity, thus confirming previous speculations based on far-infrared and 0^+ observations that substantial neutral material protrudes into the cavity and may constitute infalling matter that fuels the central activity. We show that *all* the major ionized filaments (the Western Arc, the Bar, the Northern Arm, and the Eastern Arm) are ionization fronts at the interfaces between low and high density regions, as had been previously demonstrated convincingly only for the Western Arc. The locations of these ionization fronts imply that the UV heating and ionizing sources are indeed centrally located in the cavity. The derived dust temperatures strongly support this picture: they decrease away from the region of IRS 1 and Sgr A*, and they drop abruptly where the gas density increases at the ring. Unexpectedly high dust temperatures in the dense SW molecular cloud

complex may result from a tilt of the cavity/ring boundary to our line of sight, but an alternative explanation is that a significant fraction of the UV radiation incident on the complex penetrates deeply into it. If true, individual molecular complexes in the molecular ring are porous, or clumpy, which, together with the fact that UV radiation from the **central** cluster of sources appears to **propagate** between the large molecular complexes in the SW lobe, makes it possible for the more extended molecular disk to be heated by UV radiation from the central cluster of sources in the cavity. We determine that the **total** UV luminosity emitted by the central cluster is $1.7 \pm 0.5 \times 10^7 L_{\odot}$, which agrees with our derived infrared luminosity. Half of this UV luminosity is absorbed by dust in the cavity, and more than 40% of the UV radiation that propagates to the edge of the cavity is absorbed by dust in the neutral-gas ring, which implies that the ring thickness at its inner edge is at least 0.8 pc.

1. INTRODUCTION

The infrared appearance of the central 5 pc of the Galaxy at $\lambda > 50 \mu\text{m}$ is dominated by two lobes separated along the Galactic plane by several parsecs. In contrast, the **infrared** continuum at shorter wavelengths is much more concentrated to the nuclear core (Harvey, Campbell, & Hoffmann 1976; Rieke, Telesco, & Harper 1978; **Becklin, Gatley, & Werner** 1982; Davidson et al. 1992). All of the infrared continuum radiation observed longward of a few microns is emitted by heated dust particles, and so this striking dichotomy is thought to represent a ring of cool dust encircling a central, lower-density cavity filled with hotter dust (**Becklin et al.** 1982). This model, which has been confirmed in detail, has been remarkably useful for the interpretation of the broad range of observations of the Galactic Center (see, e.g., Jackson et al. 1993 for an overview).

Infrared, sub millimeter, and radio spectroscopy of atoms and molecules shows that the cool, neutral-gas ring extends from -1.5 pc at its inner edge to at least 7 pc and that it is rotating and clumpy (e.g., Gusten et al. 1987; Jackson et al. 1993). An intense arc of ionized gas, detected in radio continuum and **Ne⁺** line emission, coincides with the ring's inner edge to the west and southwest of the nucleus. North of the nucleus, a bridge of ionized gas extends from the ring into the central cluster. These and other filamentary and diffuse features in the cavity are probably ionized by UV radiation from the cluster of sources located in the cavity (**Serabyn & Lacy** 1985). Despite the first impression that the cavity is filled only with ionized gas, Jackson et al. (1993) see neutral oxygen coincident with the northeastern **part** of the cavity. Much of this neutral gas may lie within the cavity and actually constitute most of the gas mass there (Davidson et al. 1992; Jackson et al. 1993).

The cavity contains numerous compact sources detected from 1 to 30 **μm** . Many are apparently internally heated (e.g., Smith, Aitken, & Roche 1990; **Gezari, Dwek, & Varosi** 1993), and there is strong evidence that at least a dozen of them are

blue supergiants undergoing strong mass loss (Rieke, Rieke, & Paul 1989; Allen, Hyland, & Hillier 1990; Krabbe et al. 1991). The relative roles of those stars and the putative black hole coincident with the bright nonthermal radio source Sgr A* in heating the dust and generating the luminosity of the Galactic Center are unknown, but simple assumptions about the stars indicate that they may be sufficiently luminous to provide all of the central far-infrared luminosity (e. g., Allen et al. 1990; Krabbe et al. 1991). These rare blue supergiants probably represent only a small fraction of a large number of OB stars, most of which are much less luminous than the supergiants, that formed within the last 10^6 yr in the central few parsecs of the Galaxy (Rieke et al. 1989; Krabbe et al. 1991).

The appearance of the Galactic Center is determined largely by the spatial distributions of the matter and radiation and the luminosity of the heating source(s). Infrared-emitting dust is a useful probe of these properties, because it permeates both ionized and neutral regions in rough proportion to the gas densities there, and its temperature reflects the value of the local radiation field. In this paper we present 10, 20, and 30 μm maps which provide new information about the structure and energetic of the central 5 pc of the Galaxy. They are the first infrared maps showing the thermal emission from dust particles in the cavity and the ring with both high sensitivity and an angular resolution as good as several arcsec. Almost all previous mid-infrared maps of the dust spanned only the cavity region. An exception is the 8"5-resolution, 10 μm map by Rieke, Telesco, & Harper (1978) which shows faint emission from the ring region southwest of the cavity. All other maps showing the emission from dust in both the cavity and the ring are based on airborne far-infrared observations with angular resolutions no better than $\sim 20''$ (Harvey et al. 1976, Rieke et al. 1978; Becklin et al. 1982; Davidson et al. 1992). In this paper we assume a distance of 8.5 kpc to the Galactic Center,

2. OBSERVATIONS AND PROCEDURE

We mapped the Galactic Center on UT 1992 May 3-5 using the Marshall Space Flight Center bolometer array (Big Mac) at the NASA Infrared Telescope Facility (IRTF). Maps were made at $10.8\ \mu\text{m}$ ($\Delta\lambda = 5.3\ \mu\text{m}$, FWHM), $19.2\ \mu\text{m}$ ($\Delta\lambda = 5.2\ \mu\text{m}$), and $30\ \mu\text{m}$ ($\Delta\lambda = 5\ \mu\text{m}$). The array consists of 20 square pixels arranged in a 5×4 (R.A. \times Dec.) configuration with only a small dead space between adjacent pixels. The field-of-view (FWHM) of each pixel was $3'.9 \times 4'.2$. (Although each pixel is intrinsically square, the pixel profiles are smeared by the ~ 10 Hz oscillation, or “chopping,” of the telescope secondary mirror.) The pixel center-to-center separation was $4'.5$, and the full array subtended $23'' \times 18''$. The separation between the object and sky-reference positions was $75''$ along P.A. $= 123^\circ$ (i.e., perpendicular to the Galactic Plane) for the large-scale map at $19.2\ \mu\text{m}$ and $90''$ in R. A. for all other maps (see below). We saw evidence for source flux in the sky-reference beam when we tried to extend our maps to more than about $40''$ to the northwest and southeast from IRS 1, and so data from those regions were discarded; airborne observations at $30\text{-}50\ \mu\text{m}$ (Becklin et al. 1982; Davidson et al. 1991) imply that the mid-infrared fluxes are concentrated enough in the Sgr A region that the $10\text{-}30\ \mu\text{m}$ maps we present should not be affected by flux in the sky-reference beams.

The star α Sco was used for absolute flux calibration at 10.8 and $19.2\ \mu\text{m}$, assuming flux densities of 2291 and 834 Jy, respectively, based on interpolation from values in the IRTF list of standard stars. The $30\ \mu\text{m}$ filter has a small spectral leak at $\lambda < 5\ \mu\text{m}$. Therefore, stellar standards are inappropriate for calibrating this passband, but experience shows that accurate photometry can be obtained with this filter as long as the program objects and standards have relatively “cool” spectral energy distributions; i.e., they must be relatively deficient in short-wavelength flux, which applies to the Galactic Center region discussed here. To calibrate photometrically our $30\ \mu\text{m}$ maps, obtained on UT 1992 May 4, we observed the Galilean satellite Callisto

on the same night, determining that its 10.8- to-19.2 μm color temperature was 164 K; we then took the 30 μm flux level of Callisto to be that of a 164 K blackbody normalized to the 10.8 and 19.2 μm flux densities. We estimate the uncertainties in the absolute calibration to be 7%, 10%, and 20% at 10.8, 19.2, and 30 μm , respectively, Airmass corrections at each wavelength were determined by frequent monitoring of the flux from the bright Galactic Center source IRS 1. All photometry presented in this paper has been corrected for the non-zero widths of the filter passbands assuming the average spectral energy distribution of the Galactic Center region.

Two maps were made at each of the three wavelengths 10.8, 19.2, and 30 μm : a large-scale mosaic composed of contiguous array settings spanning the central 60" x 90" of Sgr A, and a smaller, fully (Nyquist) sampled map lying within the boundaries of the larger one but concentrated primarily to the region in the southwest quadrant; the two maps at each wavelength consist of independent data. The large-scale maps are shown in Fig. 1, and the fully sampled maps are shown in Fig. 2. The contour intervals are logarithmic. To improve the signal-to-noise ratio in the lobe region of the fully sampled maps, the flux distributions there were smoothed with a 4"5 (1 pixel-sized) boxcar. The observational procedure consisted of maximizing the signal detected in a central pixel of the array on the Galactic Center source IRS 1 at 10.8 μm , after which the filter passband was changed and the telescope was offset as desired. This peaking procedure is unambiguous, because IRS 1, indicated by a cross in the figures, is compact and substantially brighter at 10.8 μm than any other source in this region (see, e.g., Becklin & Neugebauer 1975). We estimate the uncertainty in the peaking and offsetting procedures to be $\pm 1''$, which also characterizes the uncertainty in the relative positions of the different maps. The 1950 positions assumed in this paper for IRS 1 and Sgr A* are $17^{\text{h}}42^{\text{m}}29.^{\text{s}}74-28^{\circ}59'18''2$ and $17^{\text{h}}42^{\text{m}}9.^{\text{s}}32-28^{\circ}59'18''4$, respectively (see Smith et al. 1990; Eckart et al. 1992; and references therein).

3. RESULTS

3.1 *The Mid-Infrared Maps*

The large-scale maps in Fig. 1 span about $60'' \times 90''$ (R.A. \times Dec.), which corresponds to $2.5 \text{ pc} \times 3.8 \text{ pc}$. The maps at all three wavelengths show the bright central complex, which is centered near IRS 1 and Sgr A*, and a prominent ridge or lobe of emission (the “SW lobe”) extending about $50''$ to the southwest of IRS 1. In the regions of overlap, the fully sampled maps shown in Fig. 2 agree well with the large-scale maps. The fully sampled map at $10.8 \mu\text{m}$ includes only the SW lobe, whereas the 19.2 and $30 \mu\text{m}$ maps span the SW lobe and much of the region around IRS 1. Many of the prominent compact sources detected at $1.0 \mu\text{m}$ (e.g., Rieke & Low 1973; Becklin & Neugebauer 1975; Gezari et al. 1987) are indicated in the fully sampled $19.2 \mu\text{m}$ map in Fig. 2b. Discrete sources at 19.2 and $30 \mu\text{m}$ coincide within $1''$ with IRS 1, 3, and 4, and the contours extend suggestively towards IRS 2, 5, 6, and 10. Nearly all of the $10 \mu\text{m}$ sources seem to have counterparts in the fully sampled 19.2 and $30 \mu\text{m}$ maps. However, the study of these discrete sources in the **central** complex was not the primary goal of our program, and so the observational strategy, angular resolution, and subsequent analysis have not been optimized to illuminate their properties.

In Fig. 1d we show the 8.3 GHz continuum emission observed with $2''.4$ resolution (Roberts et al. 1991) which traces primarily the distribution of ionized gas, although the brightest peak is the nonthermal source Sgr A*. Generally accepted terminology, as summarized by Lacy, Achtermann, & Serabyn (1991), is also indicated. The impression is that the mid-infrared emission is distributed like the ionized gas. All the major radio features (the **Northern Arm**, the **Bar**, the **Eastern Arm**, and the **Western Arc**) have counterparts in the infrared maps; the similarity of the $30 \mu\text{m}$ and radio morphologies is particularly striking. For **example**, the **SW infrared** lobe corresponds to the southern extension of the Western Arc, of which the entire

length northward to IRS 8 is well defined at 30 μm . Our maps show clearly that the lobe consists of two dominant emission regions of comparable surface brightness. Especially at 30 μm , these two emission regions are elongated roughly along the lobe ridge. Comparison of our maps to the radio continuum emission reveals that the northern of the two dominant mid-infrared sources in the SW lobe coincides with an extended radio peak, whereas the centroid of the southern mid-infrared source is offset $\sim 4''$ to the southeast along the arc from the nearest radio peak which is also the brightest radio source in the SW lobe. We also note that the lowest contour in the SW lobe bulges noticeably to the west at 10.8 and 19.2 μm but not obviously at 30 μm . This structure is real (Section 6), but it is not evident at 30 μm , because the 30 μm sensitivity is much lower than that at the shorter wavelengths (see the Figs. 1 & 2 captions).

Although the mid-infrared and radio maps look very similar, there are subtle but important differences. In Fig. 3a we show the mid-infrared and 8 GHz flux densities along an RA scan through the SW lobe indicated by the horizontal line in Fig. 2b; the scan is roughly perpendicular to the molecular ring in this region and cuts across the boundary between the cavity and ring. The infrared data are from the fully sampled maps (Fig. 2), and the radio data were read off the 8 GHz map presented in Fig. 1d. The positions of maximum 10.8 μm and 8 GHz fluxes coincide, but with increasing wavelength there is a progressive shift of the peak emission away from the cavity. Since hotter dust dominates at shorter wavelengths, the warmest dust must be mixed with the ridge of ionized gas, and the cooler dust is located to the west and southwest. Thus, we see clear evidence for a temperature gradient in the dust across the cavity/ring boundary. The wavelength dependence of the flux seen in this scan is part of a large-scale pattern reflecting the distribution of matter and radiation throughout Sgr A which we explore further below.

The flux densities integrated within the lowest contours of our large-scale maps are 1260 ± 110 Jy at $10.8 \mu\text{m}$, 4280 ± 480 Jy at $19.2 \mu\text{m}$, and 11800 ± 2480 Jy at $30 \mu\text{m}$. The uncertainties include those in absolute calibration and data reduction. For the purposes of determining the cavity and ring flux densities separately, we indicate the two regions in Fig. 1e on an outline of the $30 \mu\text{m}$ map. This separation into cavity and ring regions is consistent both with the usual terminology used for Sgr A and the distribution of optical depth discussed below. The cavity region so defined is about $40''$ (1.7 pc) in diameter. The flux densities determined for each region are listed in Fig. 1e. We see that the ring contributes about 20 % of the total observed flux density at $10.8 \mu\text{m}$, 25% at $19.2 \mu\text{m}$, and 45% at $30 \mu\text{m}$. To determine the emitted luminosities, fairly large corrections for interstellar extinction must be applied to these values (Section 3.2). Note that integration over a $30''$ -diameter circular region centered on IRS 1 yields a $30 \mu\text{m}$ flux density of 4200 Jy, which agrees well with the value observed by Becklin et al. (1982) in a $30''$ beam.

Because of the uniqueness of our $30 \mu\text{m}$ observations, it is worthwhile to see what limits they place on the flux density of the unusual source Sgr A* (see Zylka et al. 1994 and Gezari et al. 1994 for discussions of this source and its luminosity). We consider the original grid of data from which we constructed the fully sampled $30 \mu\text{m}$ map presented in Fig. 2c. While observing this grid, a pixel of the detector array was centered at a position $O'.8$ from Sgr A*, so that the source was located fortuitously near the most sensitive part of the pixel. Nevertheless, even at Mauna Kea the noise associated with rapid changes in the sky transparency and thermal emission at $30 \mu\text{m}$ (and 1.5 airmasses) is much larger than it is at shorter wavelengths. The $30 \mu\text{m}$ flux density detected in the pixel positioned at Sgr A* is 69 ± 10 Jy, which is precisely consistent with the smooth contours shown in Fig. 2c at the location of Sgr A* (filled circle). Therefore, the contours at that location exhibit no structure that we can attribute to emission from a point source. Roughly then, we might assign a 2σ upper

limit of 20 Jy to the 30 μm flux density from Sgr A*. Although unique, this limit is not a particularly tight constraint on the spectrum of Sgr A* (see Zylka et al. 1994). From a similar analysis of our fully sampled 19.2 μm map (Fig. 2b), we derive an upper limit of 1.4 Jy, which is comparable to the more carefully derived 20 μm limit obtained by Gezari et al. (1994) from images made with much higher angular resolution than ours.

3.2 Extinction Corrections

Much of the discussion in this paper will focus on the interpretation of the infrared colors in terms of the temperatures and optical depths of the Galactic Center dust. For this interpretation to be reliable, accurate account must be taken of the large interstellar extinction, corresponding to $A_V \approx 30$, which significantly modifies the observed spectral energy distribution of the Galactic Center even at these long wavelengths, a problem not fully appreciated until recently (Gezari et al. 1993; Zylka et al. 1994). The extinction correction is particularly important for determining the emitted luminosity of the Sgr A cavity, for which the spectral energy distribution peaks in the mid-infrared and is attenuated by nearly an order of magnitude by interstellar absorption. The extinction in our mid-infrared passbands consists of an absorption continuum and the broad silicate absorption features centered near 9.7 and 19 μm (see, e.g., McCarthy et al. 1980; Mathis 1990). Explicit corrections must be made for the absorption in these silicate features; in the mid-infrared it is not sufficient to assume, as is often done at longer wavelengths, that the absorption follows a power law (i. e., $Q_\lambda \propto \lambda^{1-2}$). Smith et al. (1990) showed with 5'' resolution that the 9.7 μm feature seen in absorption toward Sgr A is actually composed of a deep absorption feature of roughly uniform depth across the source and an emission feature with a strength that depends more strongly on position, McCarthy et al. (1980) observed the 16-30 μm spectrum of the central 30'' of Sgr A and detected a broad silicate absorption feature centered near 19 μm . Their fit of the spectrum, assuming it results from hot dust in

Sgr A and cool intervening dust, implies $\tau_v(19) \approx 2.1$ at the center of the feature for the cool (interstellar) dust. McCarthy et al. (1980) assumed that the silicate emissivity is similar to that deduced for the circumstellar dust of oxygen-rich stars.

Taking $\tau_v(19) = 2.1$ at the center of the feature and assuming the emissivity varies with wavelength as indicated by McCarthy et al. (1980), we infer an average optical depth across our $19.2 \mu\text{m}$ passband of $\tau_{\text{ISM}}(19.2) = 1.9$, which means that we are detecting only 15% of the flux emitted by Sgr A even at this long wavelength. Likewise, we infer $\tau_{\text{ISM}}(30) = 0.8$ (see McCarthy et al., Fig. 3) for the flux detected in our $30 \mu\text{m}$ passband, so that we detect about 45% of the $30 \mu\text{m}$ flux emerging from the Sgr A region. To determine the extinction across our broad $10.8 \mu\text{m}$ passband, we refer to the extinction curve presented by Mathis (1990), who used silicate absorption profiles from Draine & Lee (1984). We then estimate that the average broadband absorption at $10.8 \mu\text{m}$ is 1.6 times that across the $19.2 \mu\text{m}$ band, with the result that the $\tau_{\text{ISM}}(10.8) \approx 3.0$. (Optical depths that are averages across our broad bandpasses are indicated without the subscript v . The subscript ISM distinguishes the absorption by cool intervening dust from the optical depth of warm dust in Sgr A itself.)

In this paper we will need to use estimated extinction properties of dust throughout the spectrum. The UV properties of the dust, especially in the Sgr A region, are highly uncertain. Here we consider two different extinction curves summarized by Mathis (1990): one for “diffuse dust,” for which the ratio R_v of total-to-selective extinction is typically 3.1, and one for “outer-cloud dust,” for which $R_v \approx 5.0$. Because of the proximity of the ionized cavity to the molecular ring, it seems reasonable that these two extinction relations roughly span those applicable to Sgr A, although the abundances and dust properties there maybe unusual (e.g., McCarthy et al. 1980). The key distinction between these two relationships is that, relative to the infrared extinction, the UV extinction at $0.12 \mu\text{m}$ for the outer-cloud dust is about a factor of two less than it is for the diffuse dust. We have extrapolated

the extinction curve for outer-cloud dust to $\lambda < 0.12 \mu\text{m}$ by assuming that it is identical in shape to that of the diffuse dust. Note that the extinction curves summarized by Mathis (1990) represent both absorption and scattering of radiation by dust. Although essentially negligible in the infrared, scattering is significant in the UV (see, e.g., **Draine & Lee 1984**). Our use of these extinction curves assumes, in effect, that scattering of UV photons is equivalent to their absorption, which seems justified by the fact that multiple scattering of UV photons by dust in the cavity substantially increases their chances of being absorbed there.

3.3 *Mid-Infrared Colors, Dust Temperatures, and Optical Depths*

For optically thin emission, the flux density determined from our broadband observations is $F_\nu = \tau \Omega B_\nu(T_d) \exp(-\tau_{\text{ISM}})$, where Ω ($3.9 \times 10^{-10} \text{sr}$) is the pixel size, $B_\nu(T_d)$ is the Planck spectral intensity, and τ is the optical depth of emitting dust in Sgr A. The color $R(20/30)$ is defined to be the ratio of the flux densities: $R(20/30) \equiv F_\nu(19.2 \mu\text{m})/F_\nu(30 \mu\text{m})$. We determine the temperature T_d of the mid-infrared-emitting dust from the relation:

$$R(20/30) = \tau(19.2)/\tau(30) \times B_\nu(19.2, T_d)/B_\nu(30, T_d) \times \exp[-\tau_{\text{ISM}}(19.2) + \tau_{\text{ISM}}(30)],$$

where, based on comments in the previous paragraph, $\tau(19.2)/\tau(30) = 2.4$, and the exponential absorption term equals 0.33. Figure 4 presents the temperature distributions determined from our large-scale and fully sampled maps at those positions where the values of $R(20/30)$ have a statistical significance greater than three. The correspondence between $R(20/30)$ and T_d is given in the figure caption. Knowing the dust temperature and the emitted flux density at each position, we can also derive the optical depth $\tau(30)$, shown in Fig. 5, of emitting dust along the line of sight.

4. THE DISTRIBUTION OF MASS AND IONIZATION FRONTS

The optical depth determined from our mid-infrared maps corresponds to the distribution of column density of warm dust in the central 5 pc of the Galaxy. The angular resolution is five-to-ten times better than for any previous maps of the dust

spanning this region. The global distribution of $\tau(30)$ is shown in Fig. 5a. We see an irregularly shaped region of low optical depth (0.003-0.007) surrounded by one of higher optical depth with values ranging from 0.01 in the northeast to 0.2 in the southwest. In Figs. 6a and 6b we compare the global distribution of $\tau(30)$ to the 8 GHz continuum (Roberts et al. 1991), which, except for the brightest point (Sgr A*), is thermal bremsstrahlung, and to the distribution of HCN (Wright et al. 1987, in Gusten 1987; see also Gusten et al. 1987). The region of low optical depth is dominated by emission from ionized gas, whereas the western ridge of high optical depth coincides with the inner part of the molecular ring. Although the Western Arc of ionized gas overlaps the HCN and high-optical-depth ridge, the ionized and neutral regions are clearly displaced from each other, as indicated in Fig. 3a. The highest column density of emitting dust coincides with the brightest HCN clump in the SW lobe and a concentration of neutral oxygen (Fig. 6c). The northern HCN clump in the SW lobe coincides with a high dust concentration especially evident in the fully sampled map in Fig. 5b.

These properties support the widely accepted picture of a central cavity encircled by a dense ring. The lowest values of $\tau(30)$ correspond to the central cavity of ionized gas, and the higher values are in the neutral-gas ring or close to the cavity/ring interface. The column density of mid-infrared-emitting dust across Sgr A spans nearly two orders of magnitude. Combining the gas-to-color-excess ratio for either the ρ Oph region or the diffuse interstellar medium (see Savage and Mathis 1979) with the extinction curves of outer-cloud dust or diffuse dust, respectively, we derive the relation $N(\text{H}) \approx 4 \times 10^{23} \tau(30)$, where $N(\text{H})$ is the column density of hydrogen nuclei in cm^{-2} averaged over our 4" beam. Assuming that the gas-to-dust ratio is constant throughout the Galactic Center, we infer that the hydrogen column density varies from $\sim 10^{21} \text{ cm}^{-2}$ toward the cavity to nearly 10^{23} cm^{-2} in the SW lobe. For a cavity diameter of 2 pc, the average gas density in the ionized region away from

major filaments is $\sim 300 \text{ cm}^{-2}$. If the densest blob in the SW lobe is 0.5 pc thick, then the average gas density there is $\sim 5 \times 10^4 \text{ cm}^{-3}$, whereas the average densities in other, possibly more typical, parts of the ring (e.g., the northwest) are of the order of $5 \times 10^3 \text{ cm}^{-3}$. However, detailed modeling of the HCN excitation in the ring by Jackson et al. (1993) implies that the actual gas densities are two-to-three orders of magnitude larger than these average values. Therefore, the volume filling factor of the dense gas and mid-infrared dust in the ring must be only a few percent or less, as also concluded by Jackson et al. (1993) using HCN column densities.

Although the cooler dust emitting at $100 \text{ }\mu\text{m}$ is concentrated in two lobes which are coincident with the NE and SW parts of the molecular ring (Becklin et al. 1982; Davidson et al. 1992), the maps by Davidson et al. (1992; see also Rieke et al. 1978) indicated that the northern peak of $50 \text{ }\mu\text{m}$ -emitting dust may not be located on the ring but rather between the Northern and Eastern Arms inside the cavity; however, this “displacement is comparable to the positional uncertainties of their maps. Davidson et al. (1992) concluded that, if the displacement is real, neutral material protrudes into the cavity from the northeast, and that the displacement of the $50 \text{ }\mu\text{m}$ peak from the $100 \text{ }\mu\text{m}$ one corresponds to a gradient in the temperature of the heated dust there. Our maps unambiguously confirm this speculation, showing that a higher-density tongue of material does indeed dominate the northeast quadrant of the cavity. Because we see the tongue of dust in emission at $30 \text{ }\mu\text{m}$ (i.e., we have derived the optical depth of $30 \text{ }\mu\text{m}$ -emitting dust), it must be heated by the radiation field in the cavity; it is not foreground or background emission. This tongue is not obviously correlated with molecular emission (Fig. 6b), although there is some overlap, but it does coincide with a large blob of neutral oxygen seen in $[0 \text{ I}] \text{ } 63 \text{ }\mu\text{m}$ emission (Jackson et al. 1993) and apparently cool dust emitting at $450 \text{ }\mu\text{m}$ (Dent et al. 1993), as indicated in Figs. 6c and 6d. Jackson et al. (1993) suggested that the neutral oxygen they observe toward the cavity is actually within it and may constitute most of the gas mass there. Our results

combined with those of Davidson et al. (1992) and Dent et al. (1993) give 10-450 μm color temperatures that imply external heating of the tongue by a source or sources in the cavity (Section 5).

The 30 μm optical depth across the northeast tongue is fairly uniform, although it increases by nearly a factor of five near its northern boundary where it seems to merge with the ring. The feature's 30 μm optical depth is typically 0.012, so that the hydrogen column density is $\sim 5 \times 10^{21} \text{ cm}^{-2}$, which agrees reasonably well with the 22"-diameter-beam measurements made of oxygen by Jackson et al. (1993) and with the 30"-diameter-beam measurements of $\tau(90)$ by Davidson et al. (1992). This feature probably corresponds to cool matter falling into the cavity. Because of its distinct characteristics, we refer to it as the Northern Intruder¹. As argued by Jackson et al.

¹ It is worth noting that both the global and fully-sampled (Fig. 5b) maps of $\tau(30)$ show the concentration of matter $\sim 5''$ to the west or northwest of IRS 1 that we associate with the Northern Intruder. Both maps also show matter $\sim 5''$ to the south and southwest of IRS 1. However, the maps disagree in the relationship they show between these two concentrations: in the large-scale map, the matter just south of IRS 1 is part of the Intruder, whereas, in the fully sampled map it seems to be connected to a tongue of matter that may be part of the eastern segment of the ring. As a practical issue, we consider the large-scale map shown in Fig. 5a to more accurately represent the overall structure of the Intruder, because most of the Intruder was spanned by a single setting of the detector array, which reduced deleterious effects of fluctuating sky transparency at 30 μm . In contrast, the fully sampled map was constructed from fields that were interleaved to achieve Nyquist sampling, with intervening fluctuations in the sky transparency introducing inaccuracies in the inferred structure. However, the fully sampled maps clearly confirm the existence of the Intruder. The fully sampled data

presented for the SW lobe region is not very affected by this problem, because the maps were constructed from smoothed data (see Section 2).

(1993), it is likely that neutral gas located in the cavity is infalling rather than being ejected, since gas originating in the central environment where the dynamical (i. e., mixing) time scales are short and the UV radiation is so intense would almost certainly be fully **ionized**. The Northern Intruder is therefore probably a major source of neutral gas for the cavity, enriching it and fueling the recent star formation there.

Serabyn & Lacy (1985) and others have proposed that the Western Arc of ionized gas is actually an ionization front located at the inside boundary of the **neutral**-gas ring. They proposed that this front results from the ionization by UV sources located within the cavity. Similarly, Davidson et al. (1992) speculated that the Northern Arm is an ionization front associated with higher-density gas in the region that we refer to as the Northern Intruder. Our new data permit us to substantially extend these conclusions. Fig. 6a indicates that *all* of the major ionized' filaments in Sgr A lie along the edges of high-density, high-optical-depth features. Without exception, these edges face the center of the cavity where the complex of potential heating and ionizing sources are located. Within the Western Arc itself, we see that the two ionized peaks in the SW lobe are at the inner edges of the densest clump; the northern of these two clumps is most clearly shown in Fig. 5b. (Note also that the [Ne II] 12.8 μm emission-line map by Lacy et al. 1991 shows much more clearly than the 8 GHz map presented here that the northern part of the Western Arc is a sharply defined ionization front.) The Northern Arm runs parallel with the Northern Intruder along its entire length all the way from IRS 1 to IRS 8. Especially if we consider the lowest (dashed) $\tau(30)$ contours shown in Fig. 5a, it is clear that the ionized Bar lies along the northern edge of a ridge of higher-density material that is apparently that part of the Intruder which curls westward below IRS 1 and Sgr A* toward the Western Arc;

the ionized Bar gas even appears to press up against the high-density clump located due west of Sgr A* where the Bar and Western Arc merge. The Eastern Arm is contiguous with a protrusion of high density material that may coincide with the eastern segment of the molecular ring (see Fig. 6b).

On the other hand, the fact that ionization fronts are not located everywhere also tells us something. The bay of lower ionization lying between the Northern and Eastern Arms apparently results from UV shielding of that region by the Northern Intruder; ionizing photons emitted by sources in the cavity do not propagate any farther northeastward than the Northern Arm ionization front. Since the Intruder shields the northeastern part of what is probably a nearly complete ring (Jackson et al. 1993), we must conclude that much of the Intruder lies in the plane of the ring, consistent with the proposal by Lacy et al. (1991) regarding the location of some of the ionized filaments. Likewise, the high-optical-depth region about 20'' due south of IRS 1 may be **unassociated** with an ionization front and so may also be shielded from UV radiation by the Bar region. (However, the Ne^+ map by Lacy et al. 1991 shows what may be an ionization front at the northern tip of this feature.)

These comparisons show that the ionized filaments that dominate the cavity morphology actually outline the cavity boundaries irradiated by UV radiation. In the next section we explore the distribution of dust temperature throughout the cavity and ring and find that it fits neatly into this picture.

5. THE TEMPERATURE DISTRIBUTION

The main features of the dust temperature throughout the central 5 pc of the Galaxy are most easily seen by considering the three temperature regimes $T_d = 190$ -250, 120-140, and 80-90 K. In Fig. 7 we show temperature contours from these three regimes overlaid on the map of $\tau(30)$. Each temperature regime corresponds clearly to a zone in Sgr A. Within $\sim 8''$ of Sgr A*, the temperature distribution resembles roughly that of the emission maps. The hottest dust, at 250 K, coincides with the brightest **mid-**

infrared source IRS 1. Somewhat cooler dust, at ~ 190 K, is distributed in an arc extending southwest from IRS 1 and westward along the Bar. The maps (see also Fig. 4b) show several temperature peaks, including that at IRS 2 in the Bar. These results are broadly consistent with the distribution of dust effective temperature determined for the same region with higher spatial resolution by Smith et al. (1990; see also Gezari et al, 1993) using 8.3 and 12.2 μm images. Smith et al. (1990) and others have concluded that many of the discrete sources (e.g., IRS 1 and 2) are heated internally; i. e., they are not merely density enhancements heated by an external source such as Sgr A*,

At distances of $8'' - 25''$ from IRS 1, the temperature distribution differs noticeably from those of the emission maps from which it was derived. With the exception of a tongue of higher temperature dust extending from IRS 1 toward IRS 4 to the southeast, the isothermal contours across this larger-scale region are roughly circularly symmetric. However, the center of symmetry depends on the contour level: for $T_d = 140$ K, it lies between IRS 1 and Sgr A*, whereas, for 120 K, it coincides with IRS 1 and unambiguously not with Sgr A*. At distances beyond $25''$, the dust temperatures falloff relatively smoothly with distance from IRS 1, but it is obvious that in the southwest the isothermal contours (e.g., 80-90 K) are tilted almost north-south rather than being perpendicular to the line connecting them to the cavity center near Sgr A* and IRS 1.

The comparison of T_d and $\tau(30)$ in Fig. 7 implies that the density and temperature distributions are closely coupled in a way that can be understood in the context of the picture outlined in the previous section. The arc of hottest dust (190-200 K) coincides with the ionization front(s) identified with the Bar and the southern part of the Northern Arm. The temperature of this dust is consistent with this ionization front being the closest ionized feature to the UV heating sources. The intermediate-temperature dust, at 120 K, traces almost precisely the inside edge of the

western half of the ring, as expected for external heating. Likewise, the lowest temperature contours (80-90 K) are virtually indistinguishable in shape from the iso-density contours in the SW lobe and near the high-density concentration located $\sim 30''$ north of IRS 1.

Although the hottest dust lies unambiguously at the Northern Intruder's ionization front, the intermediate-temperature contours (120- 140 K) seem to have no relationship to the Northern Intruder. Rather, they seem to trace what might be the northern and eastern inside edges of the ring. However, that explanation is probably not tenable, because, as we have already shown, the Northern Intruder effectively shields much of the matter in the northeast quadrant from the cluster's UV radiation, which accounts for the paucity of ionized gas there. It seems likely that the temperature determined for this region is that of warm dust mixed with ionized gas located at the front or rear surface of the Intruder. That gas is exposed to ionizing radiation because the cluster of sources is extended along our line of sight and so illuminates the Intruder from a range of directions, and also because the Intruder and the cluster center are not exactly in the plane of the sky. Thus, the Northern Arm ionization front is actually part of one that wraps around the front or back of the Intruder, and the dust that dominates the mid-infrared emission from the main body of the Intruder is heated mainly by radiation incident on those surfaces that are more nearly perpendicular to our line of sight. This geometry is consistent with the impression one gets by inspecting Fig. 6a; the lower 8 GHz contours of the Northern Arm radiate eastward through the Intruder as though rippling across its front or rear surface.

Some UV and visual radiation may also penetrate into the Intruder and heat the dust there. This is plausible, since $\tau(30) \approx 0.01$ across the Intruder, and the optical depth for outer-cloud dust at $\lambda \leq 0.4 \mu\text{m}$ is thus less than 2. If this also **corresponds** to the radial optical depth of the Intruder, then it is penetrated by more than 10-15% of

the radiation from the cluster that is incident on its surface. The UV radiation that illuminates the Intruder's interior can also dissociate molecules, which would account for their absence there.

We have computed the temperature distribution expected for dust that is optically thin to UV radiation from a source located near IRS 1. The UV source is assumed to have a **blackbody** spectral energy distribution with a temperature of 35000 K, which is the observed excitation temperature of gas in the Sgr A cavity. We solved the equation of radiative equilibrium with the requirement that the dust temperature be 152 K at $12''.8$ (0.53 pc). This fiducial temperature was chosen because it is the value at the positions $12''.8$ NW and $12''.8$ SW of IRS-1 which are along lines of sight most typical of the ionized gas away from the neutral gas. As discussed in Section 7, the derived luminosity of the source required to heat the dust to these temperatures is different for each of the two extinction curves (Section 3.2), but the resultant temperature distributions are essentially the same. In Fig. 8, we show the result of this calculation together with observed temperatures. The plotted symbols indicate the temperatures in the four cardinal directions and toward the southwest into the lobe region. Figure 8 demonstrates that the temperature distribution calculated for optically thin dust defines a loose upper boundary to the distribution of plotted points. We could have selected some other positions in the map where the temperatures are **noticeably** above the curve (particularly at point sources such as IRS 4 and 8), but the trends throughout the Sgr A region are well represented by the plotted points.

Temperatures can fall below those expected if the cavity itself is not optically thin to UV radiation. Indeed, in the next section we show that significant UV radiation is absorbed by dust in the cavity. However, this effect should be most **noticeable** at the cavity boundary where there is a sharp increase in the gas density. In Fig. 9 we show contours of $\tau(30)$ and, as shaded pixels, those positions at which the observed temperature is at least 10 K below the temperature predicted from the model of

optically thin UV heating by a central source. Dust particles that are much cooler than expected coincide well with regions of higher optical depth, i.e., with dense neutral material. Thus, there is a unambiguous reduction in the amount of radially propagating UV radiation at the cavity-ring boundary, an issue we address further in the next section.

6. THE PROPAGATION OF UV RADIATION IN SGR A

Consider the propagation of UV radiation through the cavity, The optical depth through the cavity is low, with $\tau(30) = 0.003$ being a typical value away from the ionization fronts and dense neutral gas. For outer-cloud dust, the UV extinction at $\sim 0.14 \mu\text{m}$, where the spectrum of a 35000 K blackbody heating source peaks, is roughly 300 times larger than the $30 \mu\text{m}$ extinction. For diffuse dust, this ratio is roughly 500. Therefore, $\tau(\text{UV}) \approx 0.8\text{--}1.5$ through the cavity, and we estimate the radial UV optical depth (e. g., from the cavity center near IRS 1 to the edge of the cavity) to be 0.4-0.8. We conclude that about 50% of the UV photons emitted in the vicinity of IRS 1 and Sgr A* actually propagate to the boundary.

The UV radiation that propagates to the cavity boundary can contribute (or dominate) the heating of gas and dust in the neutral-gas ring, and it is of interest to ask how far we expect the UV radiation to penetrate into the ring. Along the western part of the molecular ring, $\tau(30)$ ranges from ~ 0.04 in the northwest to nearly 0.2 in the southwest (Fig. 5). For outer-cloud dust, $\tau(\text{UV}) \approx 11$ and 55, respectively, along those lines of sight. The average gas density (n) in the SW lobe is $\sim 5 \times 10^4 \text{ cm}^{-3}$ (Section 4). For the more typical parts of the ring, $N(\text{H}) \approx 6 \times 10^{21} \text{ cm}^{-2}$ with corresponding densities of $\sim 4 \times 10^3 \text{ cm}^{-3}$. The physical distance AR over which $\tau(\text{UV}) = 1$ defines the cavity/ring interface thickness: $AR = N(\text{H})/(n) = (2 \times 10^{21})\tau(\text{UV})/\langle n \rangle$, for outer-cloud and ρ Oph dust (Section 4). Thus, we expect the interface to be roughly 0.02 pc (0.4'') thick toward the SW lobe and 0.15 pc (3''-4'') thick toward the northwest part of the ring. The optical depth throughout most of the Northern Intruder should be

comparable to that in the northwest part of the ring, so the penetration depth of the UV radiation into the Intruder should also be ~ 0.15 pc, corresponding to $4''$ - $5''$, or one pixel width.

Some regions at the cavity/ring interface, such as to the northwest, show temperature gradients roughly consistent with our estimates of AR, but others do not. If we examine the scans through the SW lobe presented in Fig. 3, we see that the temperature falloff is much less steep there than expected from our simple picture. In fact, the dust temperature along the diagonal scan changes monotonically from about 90 K at 1.3 pc from IRS 1 to about 63 K at 2.1 pc. The temperatures of ~ 60 K inferred for the SW lobe are the lowest in the map, but they are nevertheless unexpectedly high for dust located in a region of such high optical depth. As we proposed for the Intruder, this effect may result from there being a tilt of the cavity/ring interface to our line of sight, so that we are seeing some gas along our line of sight to the high-density lobe that is directly illuminated by the central cluster.

A more interesting, but purely speculative, alternative is that a substantial amount of UV radiation may be penetrating far into the SW cloud complex, again, as we proposed for the Intruder. To see this we assume that the UV luminosity of heating sources located at the cavity center is in the range 0.6 - $2 \times 10^7 L_{\odot}$ (Section 7). The dust temperature at $r = 2.1$ pc, which would be ~ 80 K for optically thin heating (Fig. 8), is near the observed value of 63 K if the emitted UV radiation is attenuated by an optical depth $\tau(\text{UV}) \approx 1$ - 2 . However, based on typical values of $\tau(30)$ in the SW lobe, we would expect $\tau(\text{UV}) > 10$. If the cloud is very clumpy, or porous, UV radiation can penetrate farther into it than indicated by the calculated values of AR. Our rough estimate for $\tau(\text{UV})$ implies that more than 10% of the UV radiation incident on the most prominent molecular cloud complex in the SW lobe might penetrate to several tenths of a parsec into the cloud. If the areal filling factor of this molecular gas at the inner part of the neutral-gas ring is 10%, as estimated by Jackson et al. (1993), then

penetration by UV radiation deep into the ring and even through the molecular gas is possible.

We point out that the RA scan shown in Fig. 3a indicates that the dust temperature beyond 10'' is roughly constant or at least not rapidly decreasing with distance. This sustained temperature level results mainly from the fact that the western end of that scan, like the eastern end, emerges somewhat from the high-density molecular ridge into a region of lower density that is directly exposed to UV radiation from the cavity. Both the $\tau(30)$ and HCN maps (Figs. 5b & 6b) imply that the SW lobe contains two large molecular complexes. A gap of 5''-10'' in declination separates the two complexes, and we propose that UV radiation from the central cavity passes through the gap and heats gas and dust at larger radii in the ring, including that observed at the west end of the RA scan in Fig. 3. The locally elevated dust temperature within the gap is also clearly evident in the temperature map in Fig. 4a, and it coincides with the prominent SW lobe of 450 μm emission (Fig. 6d) and a large westward ballooning of the lowest 10.8 and 19.2 μm contours (Figs. 1a & 1b). Although we cannot rule out local heating of that region by embedded sources (which might more easily explain the additional coincidence with NH_3 -clump G detected there by Jackson, Ho, & Barrett 1987), it seems most likely that we are seeing direct evidence for the propagation of UV radiation to larger radii through gaps in the larger scale cloud distribution. This effect and the possible porosity of individual cloud complexes enable UV radiation to propagate outward through the molecular ring, as suggested by Davidson et al. (1992) to account for the extended far-infrared emission from Sgr A.

7. THE LUMINOSITY OF THE CENTRAL, HEATING SOURCES

Determination of the infrared luminosity of Sgr A is complicated by the large mid-infrared extinction to the Galactic Center. We have applied the corrections for interstellar extinction discussed in Section 3.2 to the flux densities for the cavity and

ring presented in Fig. 1e. For the far-infrared fluxes of the cavity, we use the 50 and 100 μm flux densities measured by Becklin et al. (1982) for the central 30'' of Sgr A, corrected for extinction and multiplied by the factor $(40/30)^2$ to adjust their fluxes to the somewhat larger cavity area that we assume. The 10-100 μm luminosity emitted by the cavity is then $9 \times 10^6 L_{\odot}$. After correcting for interstellar extinction, Gezari et al. (1993) derive a luminosity of $5 \times 10^6 L_{\odot}$ for the central 15''-diameter region. From our 10.8 μm map we find that about half of the flux density that we attribute to the 40'' cavity arises in the region considered by Gezari et al, so that both values of the luminosity are consistent, with ours being a more complete sampling of the power emitted by the whole cavity.

We determine the infrared luminosity of the ring by subtracting the cavity flux densities discussed above from the total 50 and 90 μm flux densities observed across the Sgr A region by Davidson et al. (1992) who detected 39,500 Jy at 50 μm and “44,900 Jy at 90 μm (we assume a total 100 μm flux density equal to this 90 μm value). This spectral energy distribution is plotted in Fig. 10. The 10-100 μm luminosity emitted by the ring is then $8 \times 10^6 L_{\odot}$, and the total infrared luminosity emitted by Sgr A (cavity plus ring) is $1.7 \times 10^7 L_{\odot}$.

Let's consider the uncertainties in these observed values of the luminosity. The uncertainty in the emitted luminosity of the cavity is dominated by the uncertainty in the extinction correction, but, for the ring, it is dominated by measurement uncertainties of the far-infrared fluxes. This is because the extinction correction is large at 10-30 μm where the spectrum of the cavity peaks, but relatively small at 50-100 μm where the spectrum of the ring peaks. At 30-100 μm , we take the uncertainty in the extinction correction to be 15%, which is about half of the average value of the applied correction at 50 and 100 μm . Since the measurement and calibration uncertainty of the far-infrared fluxes is about 30%, the emitted far-infrared flux is known to roughly 35%. At shorter wavelengths, we assume that the uncertainty in the

extinction correction is characterized by our ignorance of the shape of the silicate absorption feature toward the Galactic Center. As a measure of that uncertainty we take the range of values observed toward various Galactic sources of the ratio of the visual extinction to the depth of the feature at $9.7\ \mu\text{m}$: $A_V/\tau_v(9.7) = 10\text{-}25$ (Gillett et al. 1975; Rieke 1974). Half the range in this value divided by the mean corresponds to an uncertainty of about 43%. Since nearly all (94 %) of the cavity flux is emitted at $10\text{-}30\ \mu\text{m}$, the uncertainty in the cavity luminosity is $\sim 43\%$. About 65% of the ring luminosity is emitted at $30\text{-}100\ \mu\text{m}$, and so we estimate the uncertainty in the luminosity emitted by the ring to be roughly 40%. Thus, the luminosities emitted by the cavity and ring are $9 \pm 4 \times 10^6 L_\odot$ and $8 \pm 3 \times 10^6 L_\odot$, respectively. The total for the Sgr A region is $1.7 \pm 0.5 \times 10^7 L_\odot$, where we have assumed that the uncertainties in the ring and cavity luminosities are independent since they have essentially different origins.

We have shown that the relationship of the heated dust, and the neutral and ionized gas throughout Sgr A is consistent with heating and ionization by UV radiation originating in the neighborhood of IRS 1 and Sgr A*. We now compare the observed luminosity to the UV luminosity required to heat the dust to the inferred temperatures. We assume extinction properties of the cavity dust to be those of diffuse dust, and we take the dust temperatures to be those which are fit by the curve drawn in Fig. 8 which corresponds to the temperatures of dust in radiative equilibrium with a central UV source. Points falling close to that curve tend to be associated with positions in the cavity (e. g., at $25''.5$, or $1.06\ \text{pc}$, SW of IRS 1 where $T_d = 112\ \text{K}$) rather than in the ring or Northern Intruder, where, as already discussed, UV radiation is strongly attenuated. The required luminosity is $6.0 \times 10^6 L_\odot$. If we use the extinction properties of outer-cloud dust, then the dust temperatures imply a luminosity of $1.1 \times 10^7 L_\odot$. Thus, the dust temperatures imply that the UV luminosity propagating to the edge of the cavity is $6\text{-}11 \times 10^6 L_\odot$. Since it is likely that roughly half of the UV

photons emitted near the center of the cavity are absorbed by cavity dust and emitted in the infrared (i. e., the UV intensity at 1 pc from IRS 1 is the attenuated field near the outer edge of the cavity; Section 6), we infer from the dust temperatures that the emitted infrared luminosity of the cavity is also $6-11 \times 10^6 L_{\odot}$, or $9 \pm 3 \times 10^6 L_{\odot}$, and the total UV luminosity emitted in the cavity is $1.2-2.2 \times 10^7 L_{\odot}$, or $1.7 \pm 0.5 \times 10^7 L_{\odot}$. These values agree with the cavity's observed infrared luminosity of $9 \pm 4 \times 10^6 L_{\odot}$ and the total infrared luminosity of $1.7 \pm 0.5 \times 10^7 L_{\odot}$. It is worth emphasizing this good agreement in the luminosities determined for Sgr A by essentially two independent approaches: direct observation of the infrared luminosity with a significant correction for intervening interstellar extinction, and analysis of the UV luminosity required to heat the dust to the inferred temperatures.

The UV heating sources emit about $1.7 \times 10^7 L_{\odot}$, of which roughly half ($9 \pm 3 \times 10^6 L_{\odot}$) propagates to the edge of the cavity. Within the uncertainties, as little as 40% (i.e., $[8-3 \times 10^6 L_{\odot}]/[9 \pm 3 \times 10^6 L_{\odot}] = 0.42$) or as much as 100% of the radiation escaping the cavity is absorbed in the ring. The ring does not 'subtend 4π sr at the cavity center, so the upper limit is uninteresting. For a cavity diameter of 2 pc, the lower limit corresponds to a ring thickness at its inner edge of about 0.8 pc. One's impression from the available maps of the Galactic Center at various wavelengths is that this lower limit is within the plausible range of values.

Among the primary candidate objects to provide the central UV luminosity of $1.7 \pm 0.5 \times 10^7 L_{\odot}$ are a group of about a dozen compact, broad-line "He I emission - stars" and probably an associated, but not yet detected, population of fainter OB stars distributed across the central -20" of the Galactic Center (Forrest et al. 1987; Allen, Hyland, & Hillier 1990; Krabbe, et al. 1991). Most of the He I stars are coincident with compact 2 μ m continuum sources, which supports the claim that many of these continuum peaks are internally heated (e.g., Rieke et al. 1989). These objects appear to be hot stars (mass-losing blue supergiants and/or Wolf-Rayet stars) which ionize the

helium in their winds. From data on late Ofpe/WN stars and other blue supergiants, Krabbe et al. (1991) infer that the ratio of luminosity to $2.2\ \mu\text{m}$ flux density for these stars is $8 \times 10^5 L_{\odot} \text{ Jy}^{-1}$ (adjusted to 8.7 Kpc for the Galactic Center distance). The dereddened $2.2\ \mu\text{m}$ emission from the individual objects imply luminosities in the range $0.4\text{--}5 \times 10^6 L_{\odot}$, with the total being as high as $\sim 1 \times 10^7 L_{\odot}$. Objects such as IRS 1, IRS 16-C, and IRS 16-NE, with $2.2\ \mu\text{m}$ flux densities of a few Janskys (e.g., Krabbe et al. 1991), may each emit $\sim 2 \times 10^6 L_{\odot}$.

8. SUMMARY AND CONCLUSIONS

Our maps of the $10\text{--}30\ \mu\text{m}$ emission from warm dust in the central 5 pc of the Galaxy have permitted us to draw the following conclusions about the energetic and the distribution of neutral and ionized gas in the Sgr A cavity and the inner part of the molecular ring.

1. The $30\ \mu\text{m}$ optical depth indicates that the dust and gas are distributed in a **low-density** cavity, with an average gas density away from filaments of $\sim 300\ \text{cm}^{-2}$, bordered by a high-density ridge with average gas densities as high as $10^5\ \text{cm}^{-2}$. The cavity and ridge correspond to the well-known ionized cavity and the inner part of the neutral-gas ring, respectively. We also see a bridge of warm dust that extends into the center of the cavity from the northern part of the ring. Because the dust associated with this bridge, which we call the Northern Intruder, is heated by radiation in the cavity, we confirm previous speculations that it actually protrudes into the cavity and that it is therefore probably falling into the cavity and fueling star formation there.
2. By comparing the distribution of warm dust mass to the 8 GHz thermal **bremsstrahlung** emission, we show that *all* the major ionized filaments (the Western Arc, the Northern Arm, the Bar, and the Eastern Arm) in the cavity are actually ionization fronts at the interfaces between the low density cavity and the **high-density** regions defined by the neutral-gas ring and the Northern Intruder. This relationship is most dramatic for the Northern Intruder which completely bisects the cavity and is

contiguous with Northern Arm and Bar. The locations of these ionization fronts and the distributions of dust temperatures imply that the UV heating and ionizing sources are centrally located in the cavity, as previously proposed.

3. The dust temperatures decrease away from the center of the cavity and show a significant drop near the interfaces of the cavity **and** the higher-density regions, as expected generally from external heating of dense clouds. However, in some dense regions, particularly the SW molecular cloud complex, the dust temperatures appear to be higher than expected for such dense regions. This effect may result from there being a tilt of the cavity/ring boundary to our line of sight. An alternative explanation is that UV radiation penetrates deeply into those cloud complexes because the clouds are clumpy, or porous. This small-scale cluminess and the easily observed **larger**-scale cluminess permit UV photons from the cavity to propagate far out into the molecular ring,

4. After correcting the observed flux densities for interstellar extinction, we estimate that the infrared luminosities emitted by the cavity and ring are $9 \pm 4 \times 10^6 L_{\odot}$ and $8 \pm 3 \times 10^6 L_{\odot}$, respectively, and the total infrared luminosity is $1.7 \pm 0.5 \times 10^7 L_{\odot}$. Depending on the assumed wavelength-dependence of the extinction, the dust temperatures near the edge of the cavity require that the UV heating flux there correspond to a luminosity of $6-11 \times 10^6 L_{\odot}$, or $9 \pm 3 \times 10^6 L_{\odot}$. Since we estimate that about half of the UV photons emitted by sources near the cavity center are absorbed by dust in the cavity, the implied total UV luminosity emitted by sources powering the Sgr A region is $1.7 \pm 0.5 \times 10^7 L_{\odot}$. Thus, the observed infrared luminosities are comparable to those emitted by the cluster of UV sources and absorbed by the cavity dust, Within the uncertainties, all, or as little as -40%, of **the UV** radiation that propagates to the edge of the cavity is absorbed by the **neutral-gas** ring. The lower limit corresponds to a ring thickness of 0.8 pc if the inner diameter of the ring is 2 **pc**.

ACKNOWLEDGMENTS

It is a pleasure to acknowledge Robert Zylka and Peter Mezger who emphasized to us the importance of interstellar extinction to Sgr A even at mid-infrared wavelengths. C. M. T. particularly wishes to thank Rudolf Decher and Carl Benson of MSFC who contributed much to the development and operation of Big Mac over the years. We also thank the IRTF staff for their continued support. Portions of this work were carried out at the Jet Propulsion Laboratory, which is operated by the California Institute of Technology under contract to the National Aeronautics and Space Administration.

REFERENCES

- Aannestad, P.A. 1975, *ApJ*, 200, 30
- Allen, D. A., Hyland, A. R., & Hillier, D.J. 1990, *MNRAS*, 244, 706
- Becklin, E. E., Gatley, I., & Werner, M. W. 1982, *ApJ*, 258, 135
- Becklin, E. E., & Neugebauer, G. 1975, *ApJ*, 200, L71
- Davidson, J. A., et al. 1992, *ApJ*, 387, 189
- Dent, W. R. F., Mathews, H. E., Wade, R., & Duncan, W. D. 1993, *ApJ*, 410, 650
- Draine, B. T., & Lee, H. M. 1984, *ApJ*, 285, 89
- Forrest, W. J., Shure, M. A., Pipher, J. L., & Woodward, C. E. 1987, in *AIP Conf. Proc. No. 155, The Galactic Center*, ed. D. C. Backer (New York: AIP), 153
- Gatley, I. 1982, in *AIP Conf. Proc. No. 83, The Galactic Center*, ed. G. R. Riegler & R. D. Blandford (New York: AIP), 25
- Gatley, I., Becklin, E. E., Werner, M. W., & Wynn-Williams, C. G. 1977, *ApJ*, 216, 277
- Gezari, D., Dwek, E., & Varosi, F. 1993, preprint
- Gezari, D., Ozemoy, L., Varosi, F., McCreight, C., & Joyce, R. 1994, in *The Nuclei of Normal Galaxies: Lessons from the Galactic Center*, eds. R. Genzel & A. I. Harris (Dordrecht: Kluwer), in press
- Gezari, D. Y., et al. 1987, in *AIP Conf. Proc. No. 155, The Galactic Center*, ed. D. C. Backer (New York: AIP), 146
- Gillett, F. C., Kleinmann, D. E., Wright, E. L., & Capps, R. W. 1975, *ApJL*, 198, L65
- Gusten, R. 1987, in *AIP Proc. 155, The Galactic Center*, ed. D. C. Backer (New York: AIP), 103
- Gusten, R., Genzel, R., Wright, M. C. H., Jaffe, D. T., Stutzki, J., & Harris, A. I. 1987, *ApJ*, 318, 124

- Hanner, M. S., Tokunaga, A. T., Golisch, W. F., Griep, D. M., & Kaminski, C. D.
1987, A&A, 187, 653
- Harvey, P. M., Campbell, M. F., & Hoffmann, W. 1'.1976, ApJ, 241, L183
- Jackson, J. M., et al. 1993, ApJ, 402, 173
- Jackson, J. M., Ho, P. T. P., & Barrett, A. H. 1987, in AIP Conf. Proc. No. 155,
The Galactic Center, ed. D. C. Backer (New York: AIP), 99
- Krabbe, A., Genzel, R., Drapatz, & Rotaciuc, V. 1991, ApJL, 382, L19
- Lacy, J. H., Achtermann, J. M., & Serabyn, E. 1991, ApJL, 380, L71
- Mathis, J. S. 1990, ARAA, 28, 37
- McCarthy, J. F., Forrest, W. J., Briotta, D. A., & Houck, J. R. 1980, ApJ, 242, 965
- Rieke, G. H. 1974, ApJL, 193, L81
- Rieke, G. H., & Low, F. J. 1973, ApJ, 184, 415
- Rieke, G. H., Rieke, M. J., & Paul, A. E. 1989, ApJ, 336, 752
- Rieke, G. H., Telesco, C. M., & Harper, D. A. 1978, ApJ, 220, 556
- Roberts, D. A., Goss, W. M., van Gorkom, J. H., & Leahy, J. P. 1991, ApJL, 366,
L15
- Savage, B. d., & Mathis, J. S. 1979, ARAA, 17, 73
- Serabyn, E., & Lacy, J. 1985, ApJ, 293, 445
- Smith, C. H., Aitken, D. K., & Roche, P. F. 1990, MNRAS, 246, 1
- Telesco, C. M., Becklin, E. E., & Wynn-Williams, C. G. 1980, ApJL, 241, L69
- Telesco, C. M., & Knacke, R. 1?. 1991, ApJL, 372, 1.29
- Wardel, M., & Yusef-Zadeh, Y. 1992, Nature, 357, 308
- Werner et al, 1976, ApJ, 204, 420
- Zylka, R., Mezger, P. G., Ward-Thomson, D., Duschl, W., & Lesch, H. 1994,
A&A, in press

FIGURE CAPTIONS

Fig. 1. (a) Large-scale map of the Galactic Center at $10.8\ \mu\text{m}$. The cross and the filled circle indicate the position of IRS 1 and Sgr A*, respectively. Contour levels (**Jy/pixel**) are logarithmically spaced at 0.5, 1, 2, 4, 8, 16, 32, and 64, with an uncertainty (standard deviation of the measured mean value) of 0.1. The peak intensity (at IRS 1) is 116 **Jy/pixel**. (b) Large-scale map at $19.2\ \mu\text{m}$. Contour levels (**Jy/pixel**) are logarithmically spaced at 2, 4, 8, 16, 32, 64, 128, and 256, with an uncertainty of 0.5. The peak intensity is 274 **Jy/pixel**. (c) Large-scale map at $30\ \mu\text{m}$. Contour levels (**Jy/pixel**) are logarithmically spaced at 28, 39, 55, 77, 108, 150, 210, and 295, with an uncertainty of 10. The peak intensity is 296 **Jy/pixel**. (d) Map of 8 GHz continuum by Roberts et al. (1991) made with a resolution of $2''.4$. The brightest point is the **nonthermal** source Sgr A*. Contour levels (**mJy/beam**) are 30, 50, 70, 90, 110, 150, 200, 300, 500, and 700, with an rms uncertainty of 0.4. (e) The cavity and ring regions, defined by thin lines, overlaid on an outline of the $30\ \mu\text{m}$ map (thick lines). The figure indicates the total observed flux densities from **each** region.

Fig. 2. Fully sampled mid-infrared maps, with logarithmically spaced contours. The cross and filled circle indicate IRS 1 and Sgr A*, respectively, (a) Map at $10.8\ \mu\text{m}$ of the SW lobe region. Contour levels (**Jy/pixel**) are 0.9, 1.2, 1.5, 2.0, 2.6, 3.4, and 4.4, with an uncertainty of 0.1. (b) Map at $19.2\ \mu\text{m}$ of cluster and SW lobe regions. Contour levels (**Jy/pixel**) are 4, 5, 7, 9, 12, 15, 20, 26, 33, 43, 56, 74, 96, 124, 161, 209, and 271, with an uncertainty of 0.5 in the cluster region and 0.3 in the SW lobe. The peak intensity is 274 **Jy/pixel**. The locations of the most prominent $10\ \mu\text{m}$ cluster sources are indicated by their IRS numbers. The dashed lines in the **SW lobe** correspond to the scan paths discussed in Fig. 3. (c) Map at $30\ \mu\text{m}$ of the cluster and SW lobe regions. Contour levels (**Jy/pixel**) are 34, 44, 58, 74, 100, 126, 163, 212,

and 276, with an uncertainty of 10 Jy in the cluster region and 5 Jy in the SW lobe. The peak intensity is 290 Jy/pixel.

Fig. 3. Scans through the SW lobe showing the distributions of 10.8, 19.2, and 30 μm flux densities, color $R(20/30)$, and optical depth $\tau(30)$. The scan paths are constructed from data in the fully sampled maps and are indicated by the dashed lines in Fig. 2b. Also shown in Panel a is a scan of the 8 GHz continuum, as extracted from the map of Roberts et al. (1991). The flux densities are normalized to the value 100 at O⁺ displacement, $R(20/30)$ and $\tau(30)$ are normalized as indicated in the figure, and the amplitude for the 8 GHz scan is in units of mJ y/beam.

Fig. 4. The dust temperature T_d derived from the 19.2 and 30 μm maps after correction for interstellar extinction. (a) Distribution based on large-scale maps. The contour levels, in Kelvins, are 70, 75, 80, 85, 90, 100, 120, 140, 160, 180, 190 (dashed), 200, 220, and 240. (b) Distribution based on the fully sampled maps. Contours are labeled by the dust temperature in Kelvins. The correspondence between T_d and $R(20/30)$ is 60(0.034), 70(0.062), 80(0.10), 90(0.15), 100(0.20), 120(0.31), 140(0.43), 160(0.52), 180(0.63), 200(0.73), 220(0.81), and 240(0.89), where we use the format $T_d(R)$.

Fig. 5. The optical depth $\tau(30)$ of dust emitting at 30 μm . (a) Distribution based on data from the large-scale maps. The contour levels, in units of 10^{-3} , are 6 (dashed), 8, 10, 20, 40, 60, 80, 100, 150, and 200. (b) Distribution based on data from the fully sampled maps. Contours are labeled by the optical depth multiplied by 10^3 .

Fig. 6. Comparison of the distribution of $\tau(30)$ (shaded area) derived from the **large-scale** maps to: (a) 8 GHz continuum (2'.4 beam; Roberts et al. 1991); (b) HCN J = 1-0

emission (3'' beam; Wright et al. 1987, in Gusten 1987). For clarity, some HCN contours are not shown; (c) [0 I] 63 μ m line emission (22'' beam; Jackson et al. 1993); (d) 450 μ m continuum emission (7'.2 beam; Dent et al. 1993). For clarity, some 450 μ m contours are not shown.

Fig. 7. Comparison of selected dust temperature contours from Fig. 4a to the distribution of optical depth (Fig. 5a). The temperature contours, in Kelvins, are 80, 90, 120, 140, 190, and 200.

Fig. 8. Observed dust temperatures (symbols) as a function of distance from IRS 1 in the cardinal directions and to the southwest. The curve represents the distribution of temperature expected for optically thin dust heated by a UV source located near IRS 1. The equation of radiative equilibrium has been solved with the requirement that the dust temperature be 152 K at 12".8 from IRS 1.

Fig. 9. The shaded pixels indicate the positions at which the observed dust temperatures are at least 10 K below the temperatures predicted by the model of optically thin UV heating by a central source. The contours indicate regions of higher optical depth in emitting dust (Fig. 5a).

Fig. 10. The spectral energy distributions of the cavity and the ring after correction for interstellar extinction, These are used to compute the luminosities discussed in the text. The 10-30 μ m data are from the present work, and the far-infrared data are from Becklin et al. (1982) and Davidson et al. (1991); see text.

emission (3'' beam; Wright et al. 1987, in Gusten 1987). For clarity, some HCN contours are not shown; (c) [0 I] 63 μ m line emission (22'' beam; Jackson et al. 1993); (d) 450 μ m continuum emission (7".2 beam; Dent et al. 1993). For clarity, some 450 μ m contours are not shown.

Fig. 7. Comparison of selected dust temperature contours from Fig. 4a to the distribution of optical depth (Fig. 5a). The temperature contours, in Kelvins, are 80, 90, 120, 140, 190, and 200.

Fig. 8. Observed dust temperatures (symbols) as a function of distance from IRS 1 in the cardinal directions and to the southwest. The curve represents the distribution of temperature expected for optically thin dust heated by a UV source located near IRS 1. The equation of radiative equilibrium has been solved with the requirement that the dust temperature be 152 K at 12'.8 from IRS 1.

Fig. 9. The shaded pixels indicate the positions at which the observed dust temperatures are at least 10 K below the temperatures predicted by the model of optically thin UV heating by a central source. The contours indicate regions of higher optical depth in emitting dust (Fig. 5a).

Fig. 10. The spectral energy distributions of the cavity and the ring after correction for interstellar extinction, These are used to compute the luminosities discussed in the text. The 10-30 μ m data are from the present work, and the far-infrared data are from Becklin et al. (1982) and Davidson et al. (1991); see text.

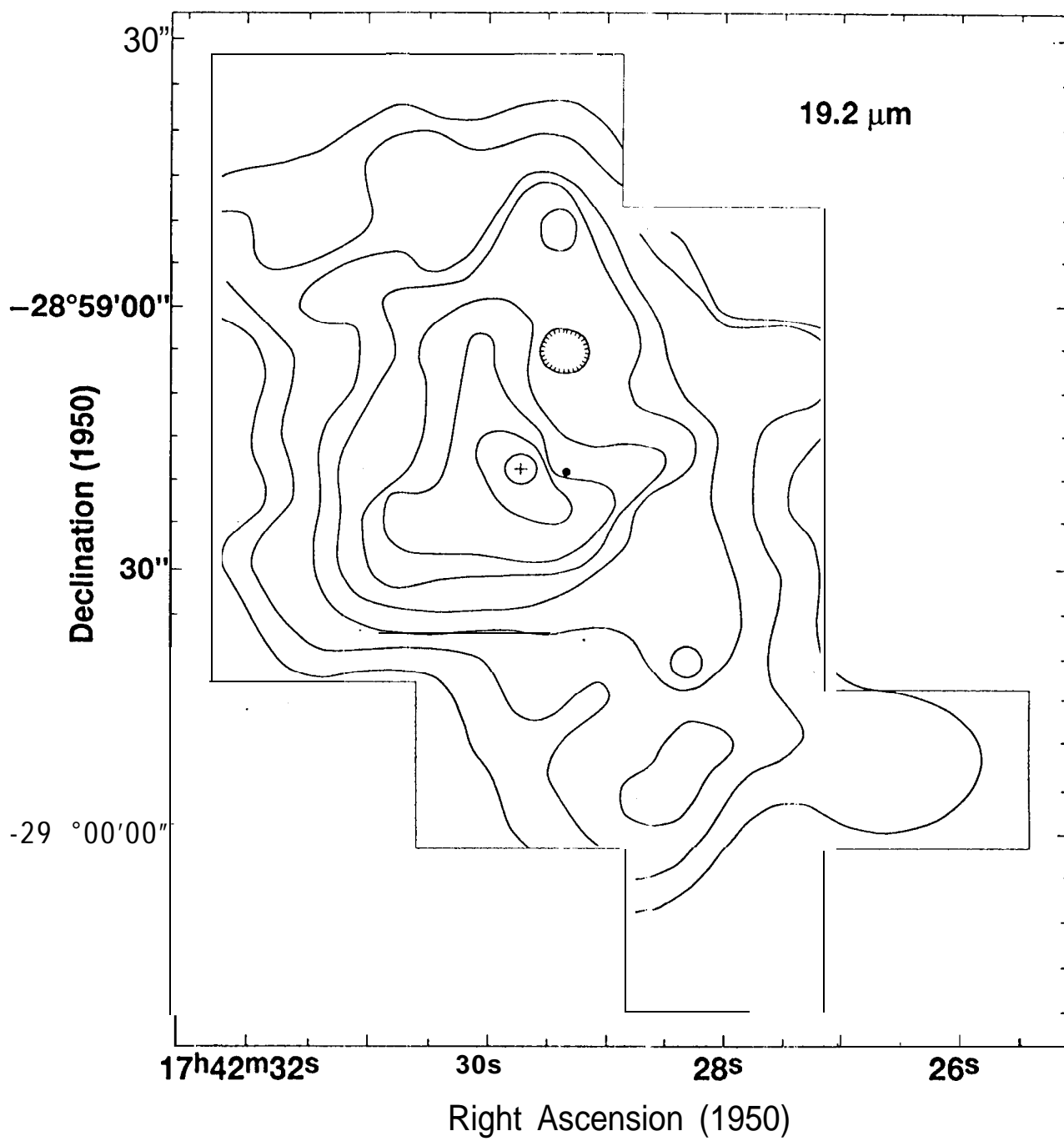


Fig. 1b

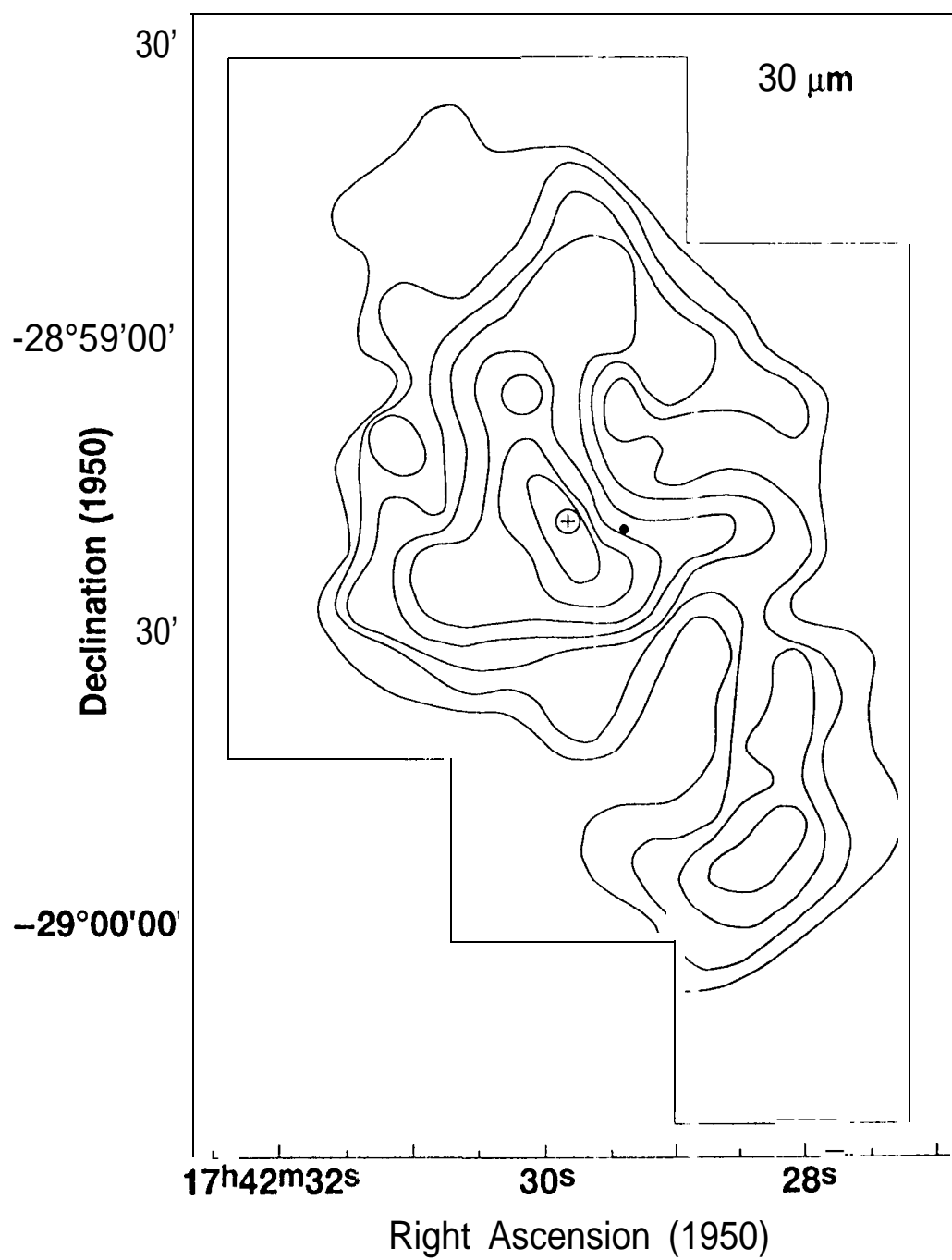


Fig. 1c

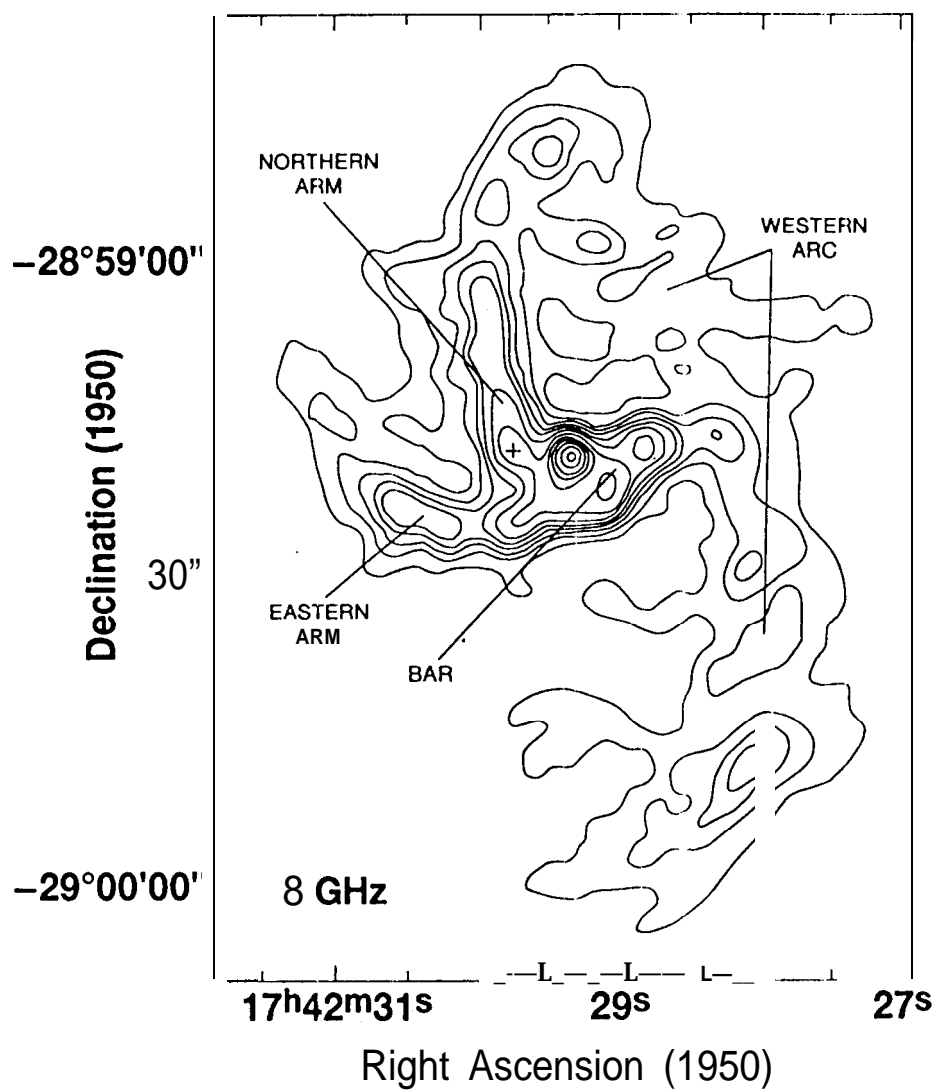


Fig. 1d

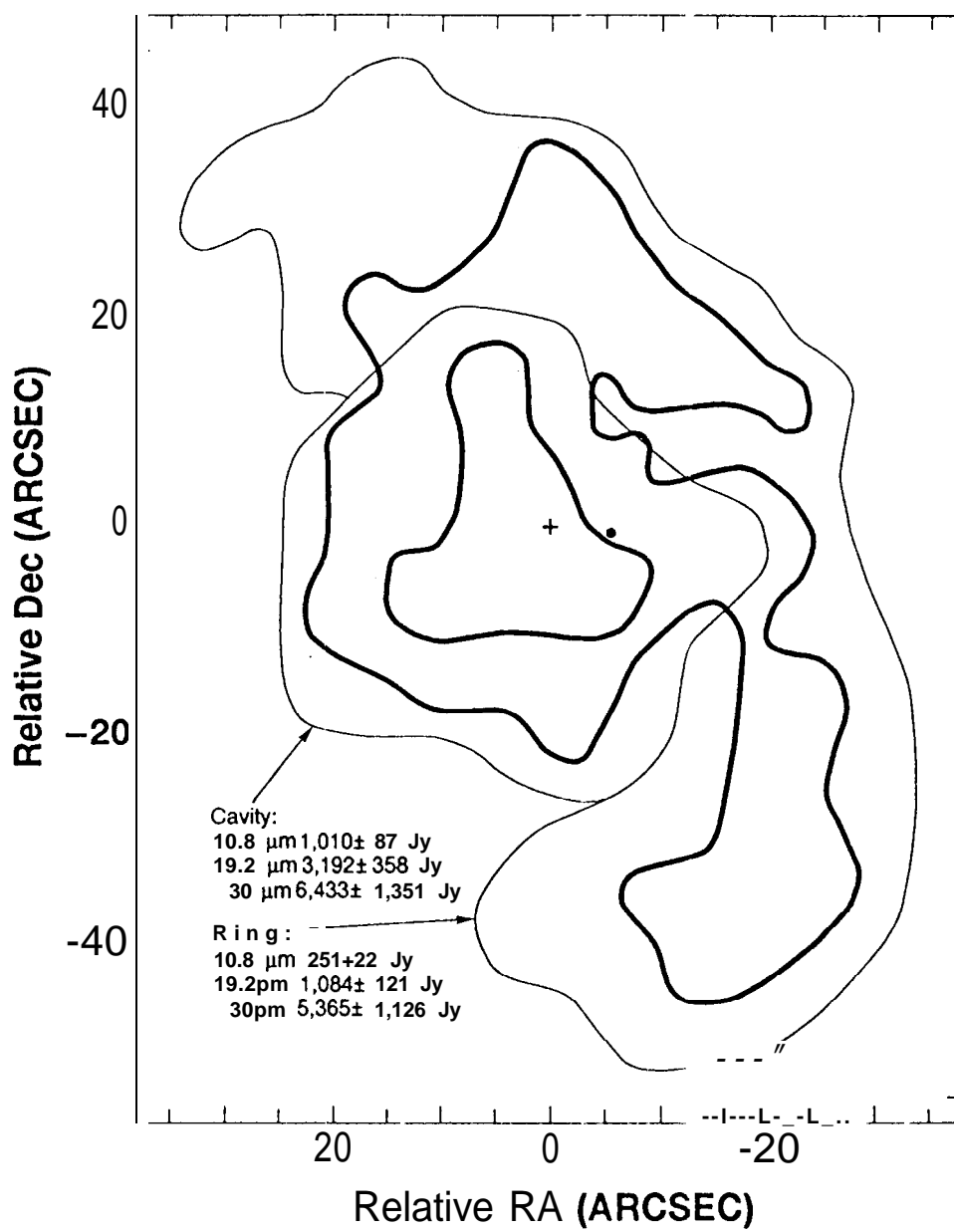


Fig. 1e

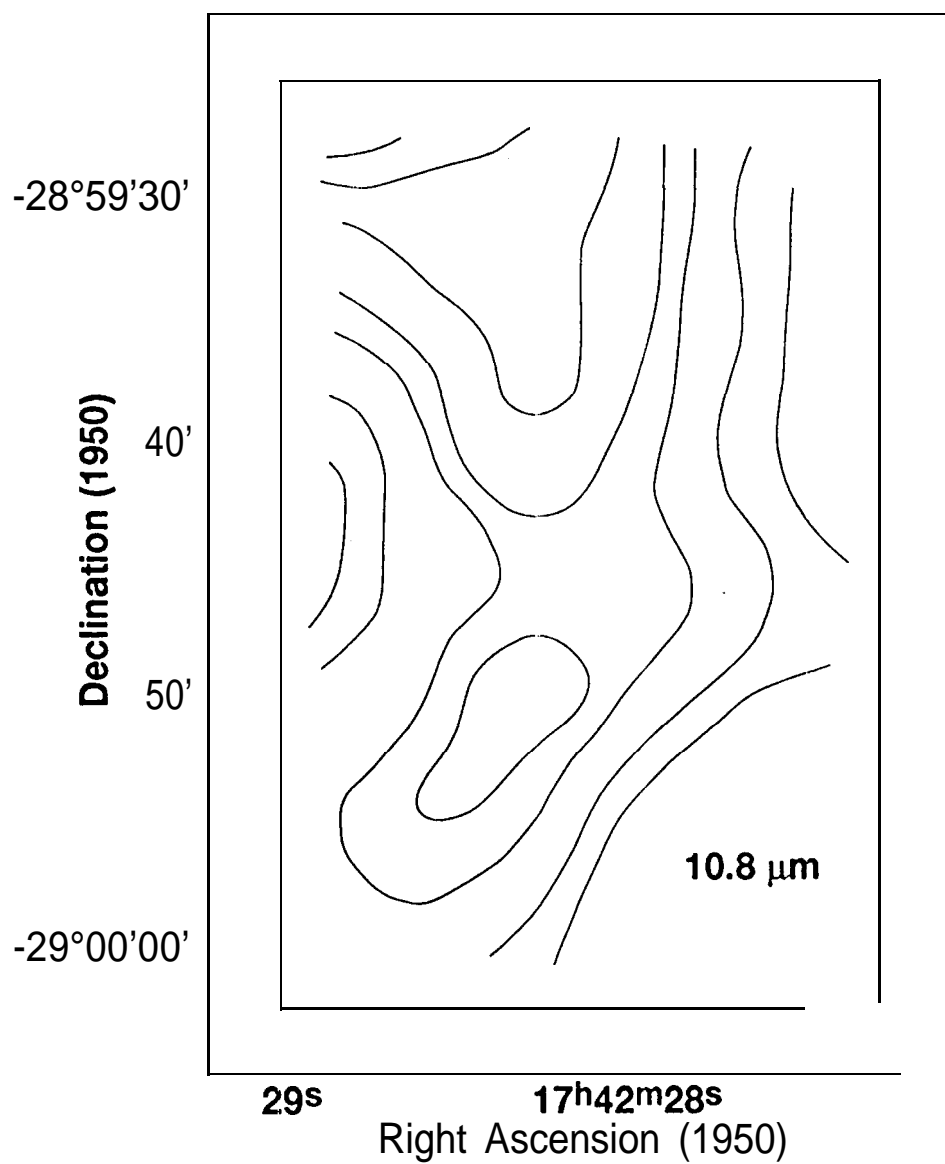


Fig. 2a

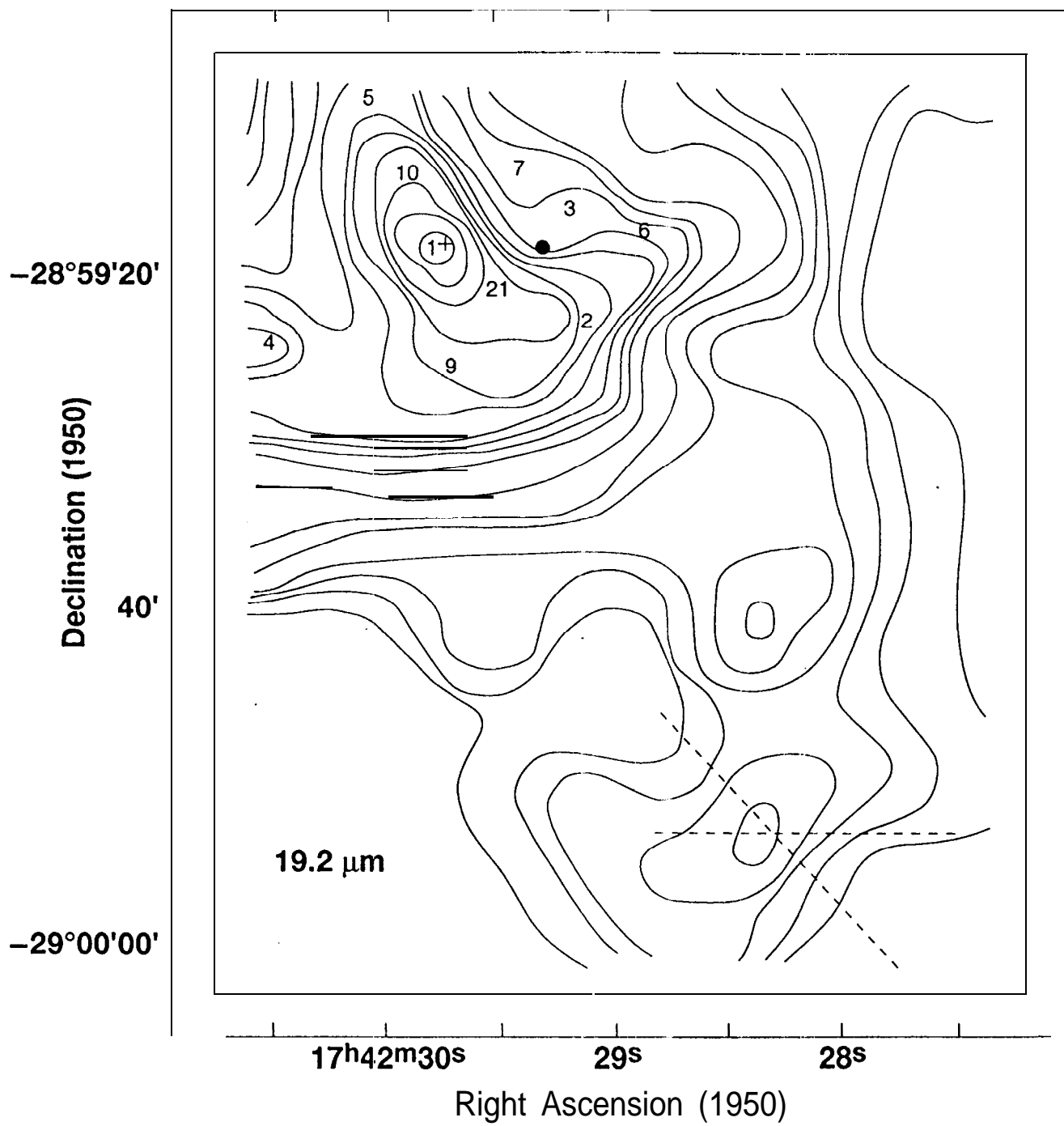


Fig. 26

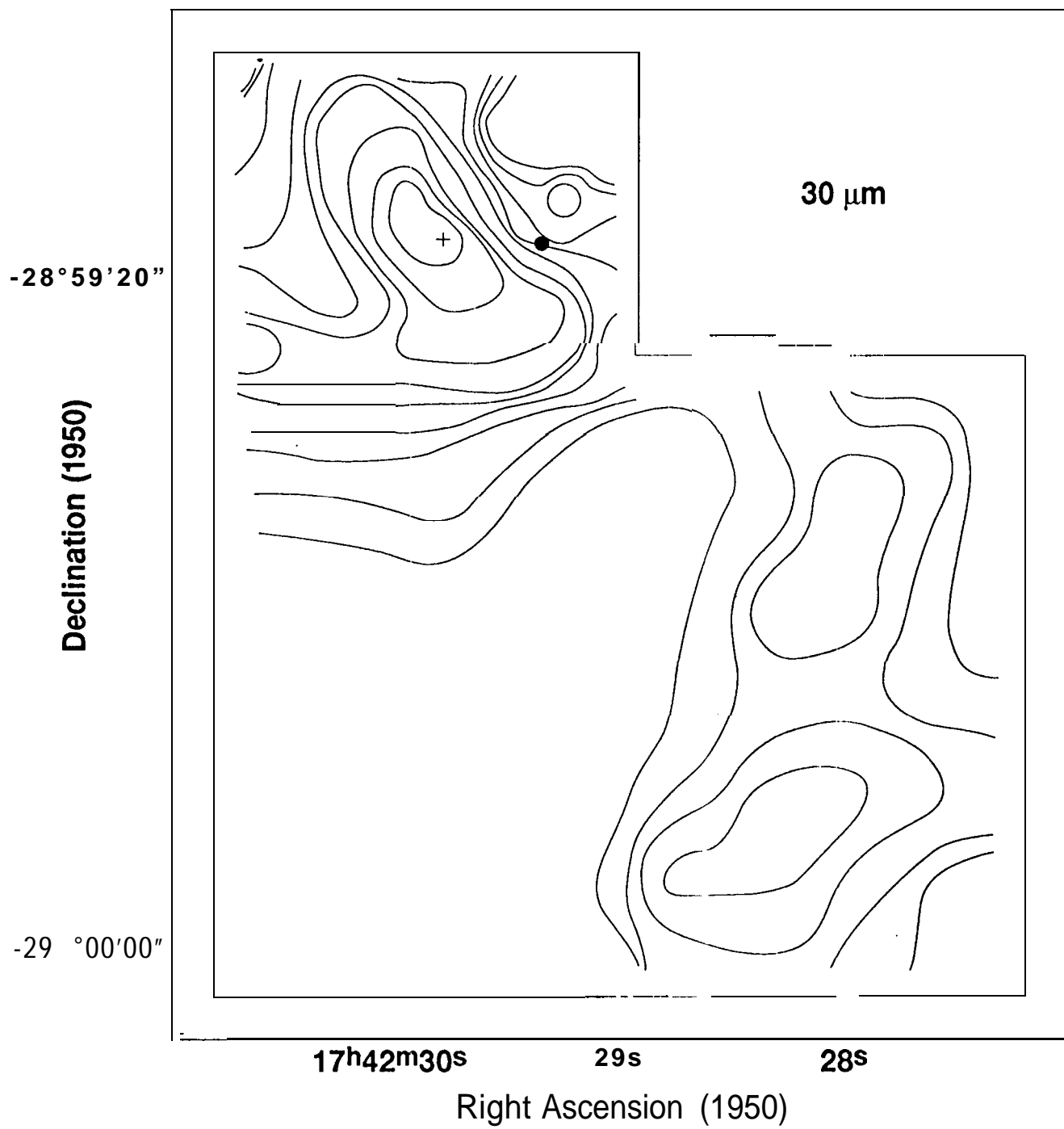
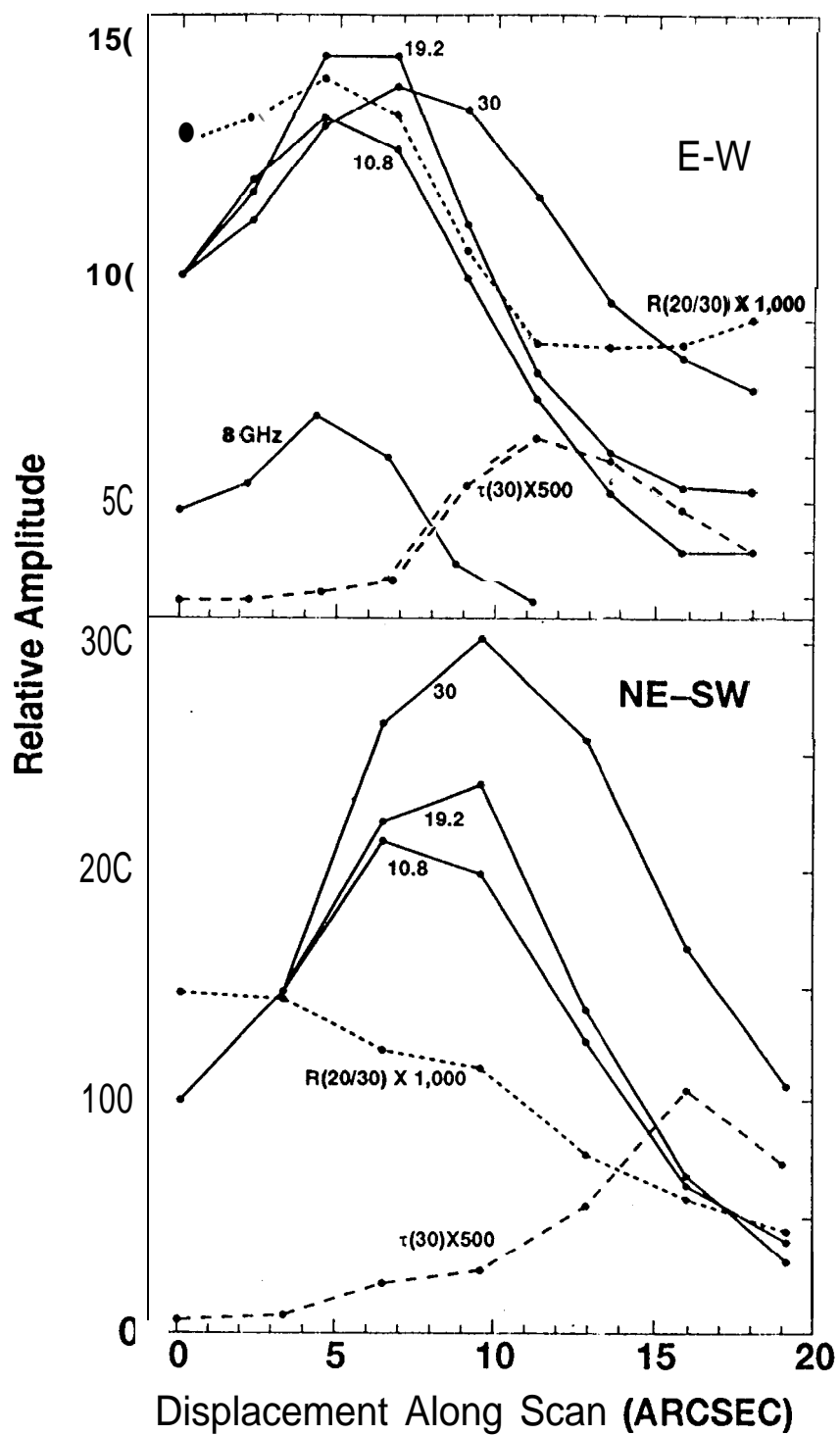


Fig. 2c



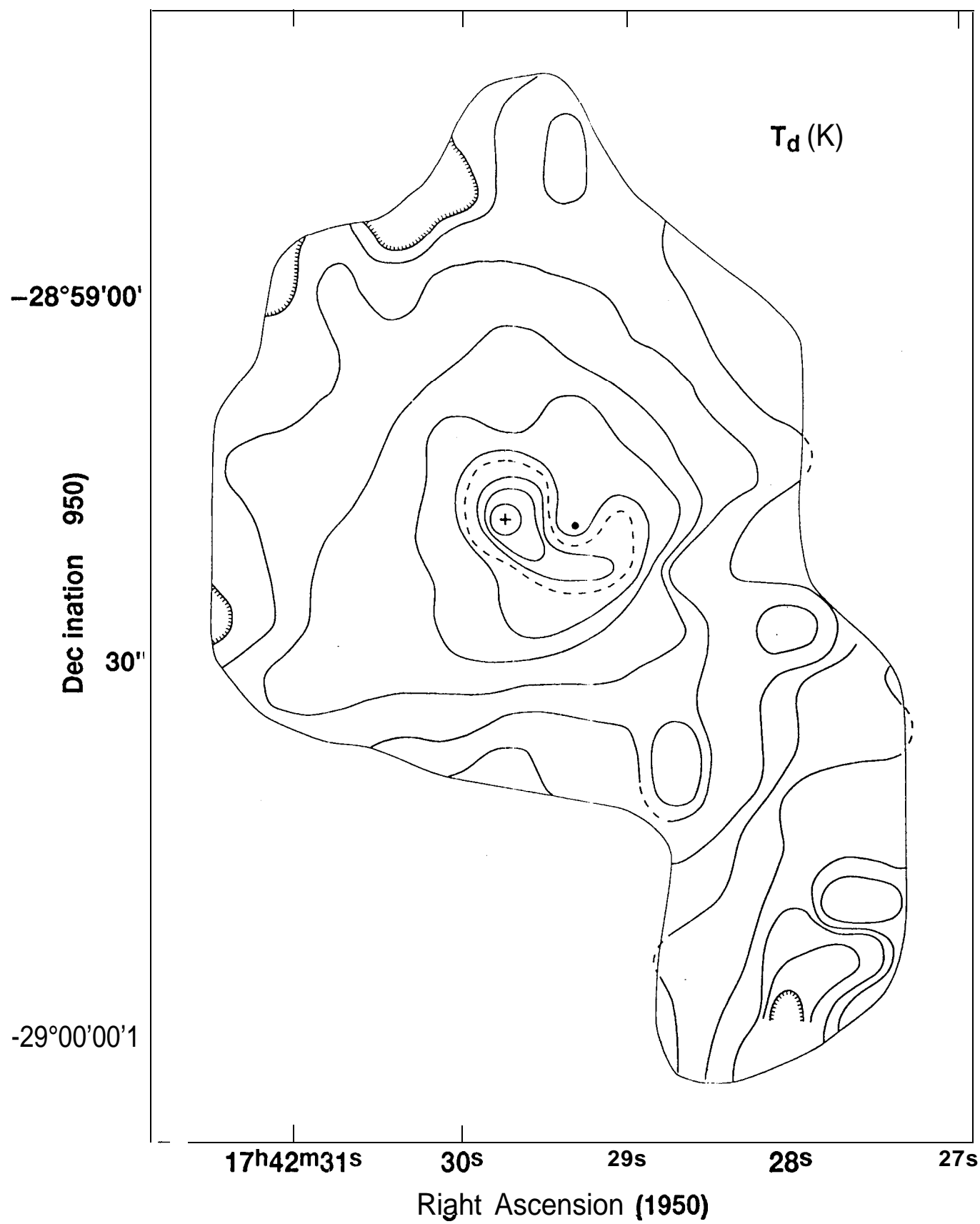


Fig. 4a

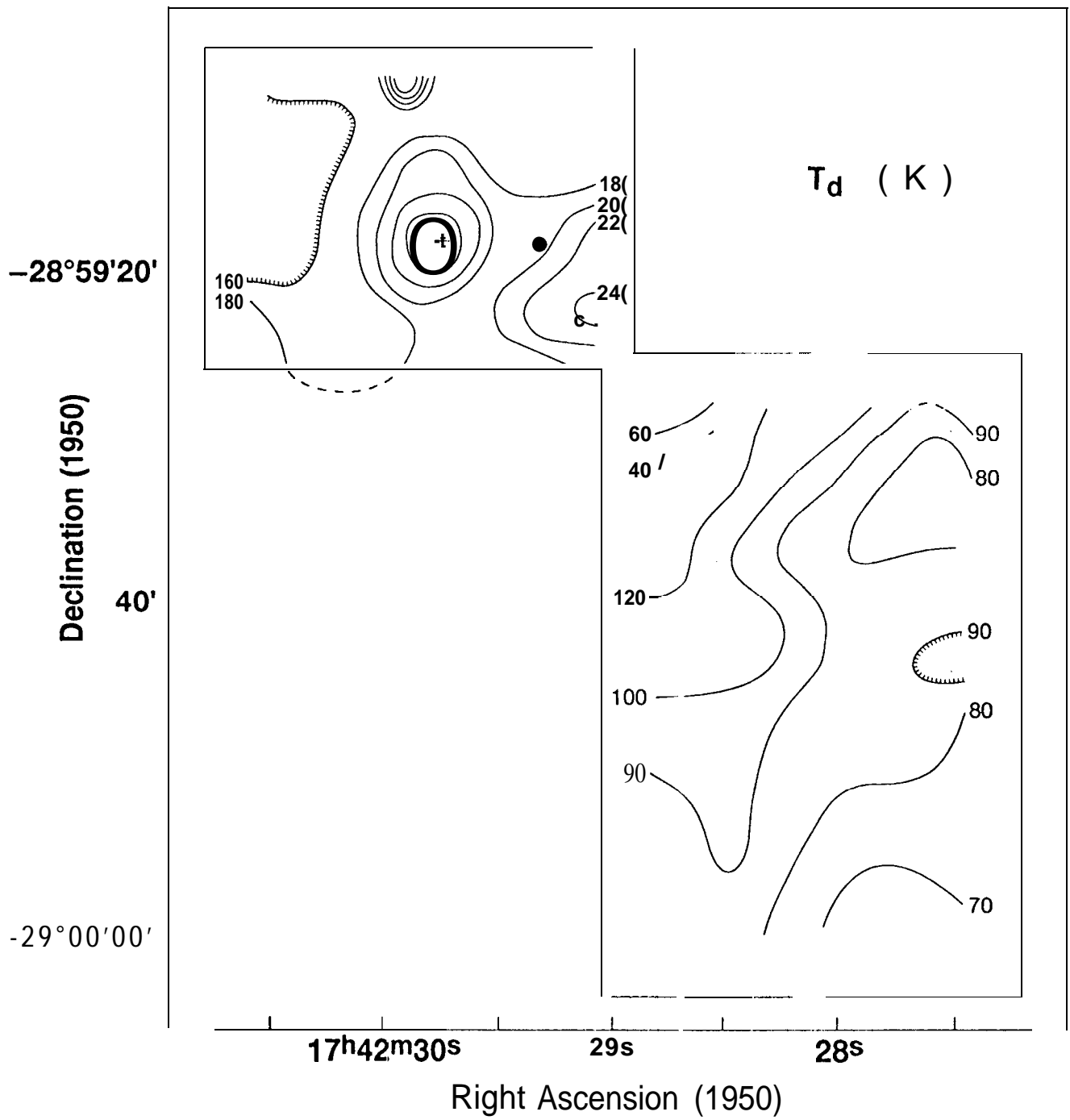


Fig. 4b

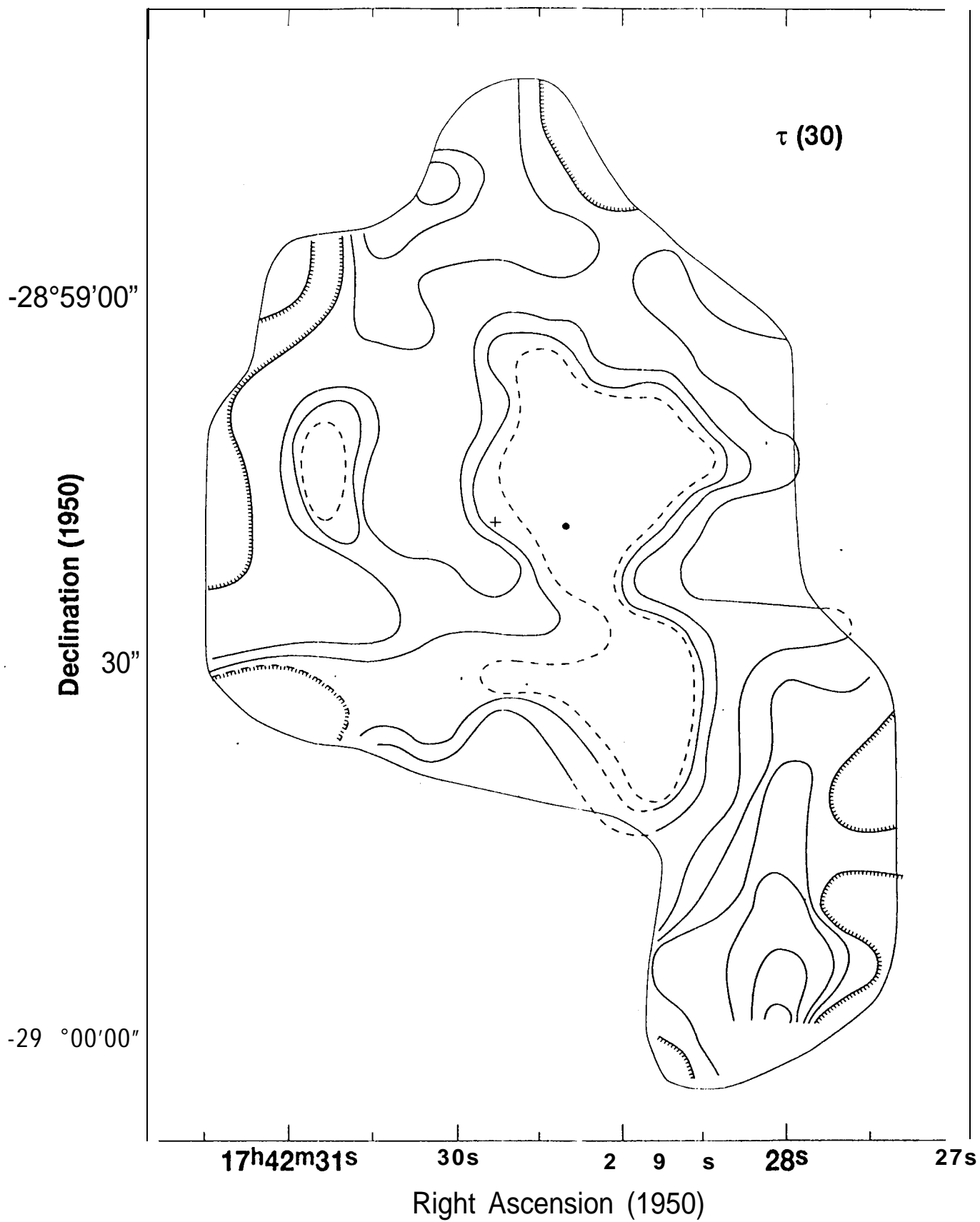
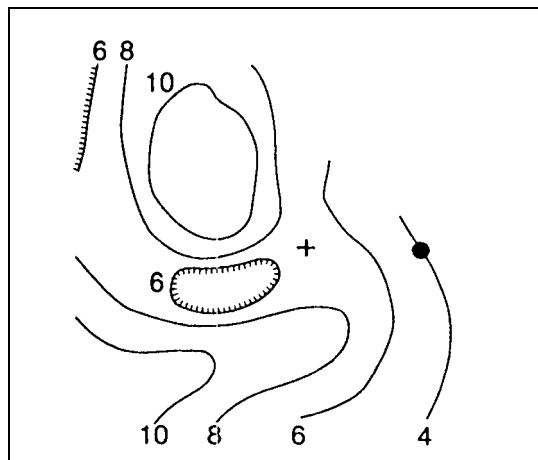


Fig 5a

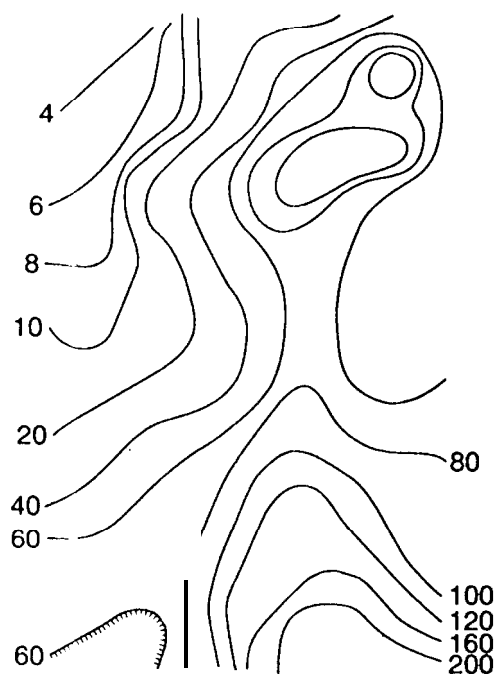
-28°59'20"

Declination (1950)

-29°00'00"



$\tau(30) \times 103$



17h42m30s

29s

28s

Right Ascension (1950)

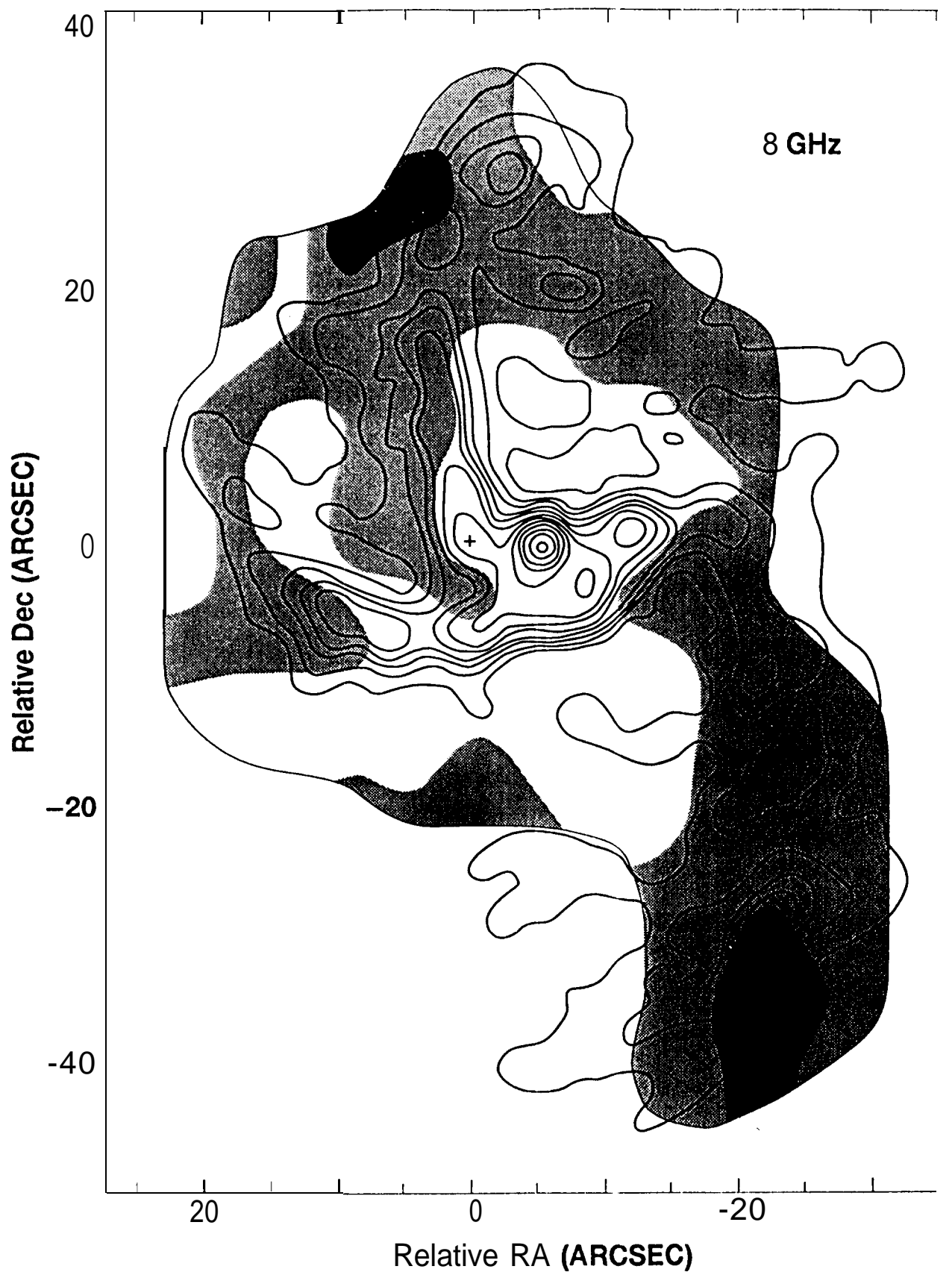


Fig. 6a

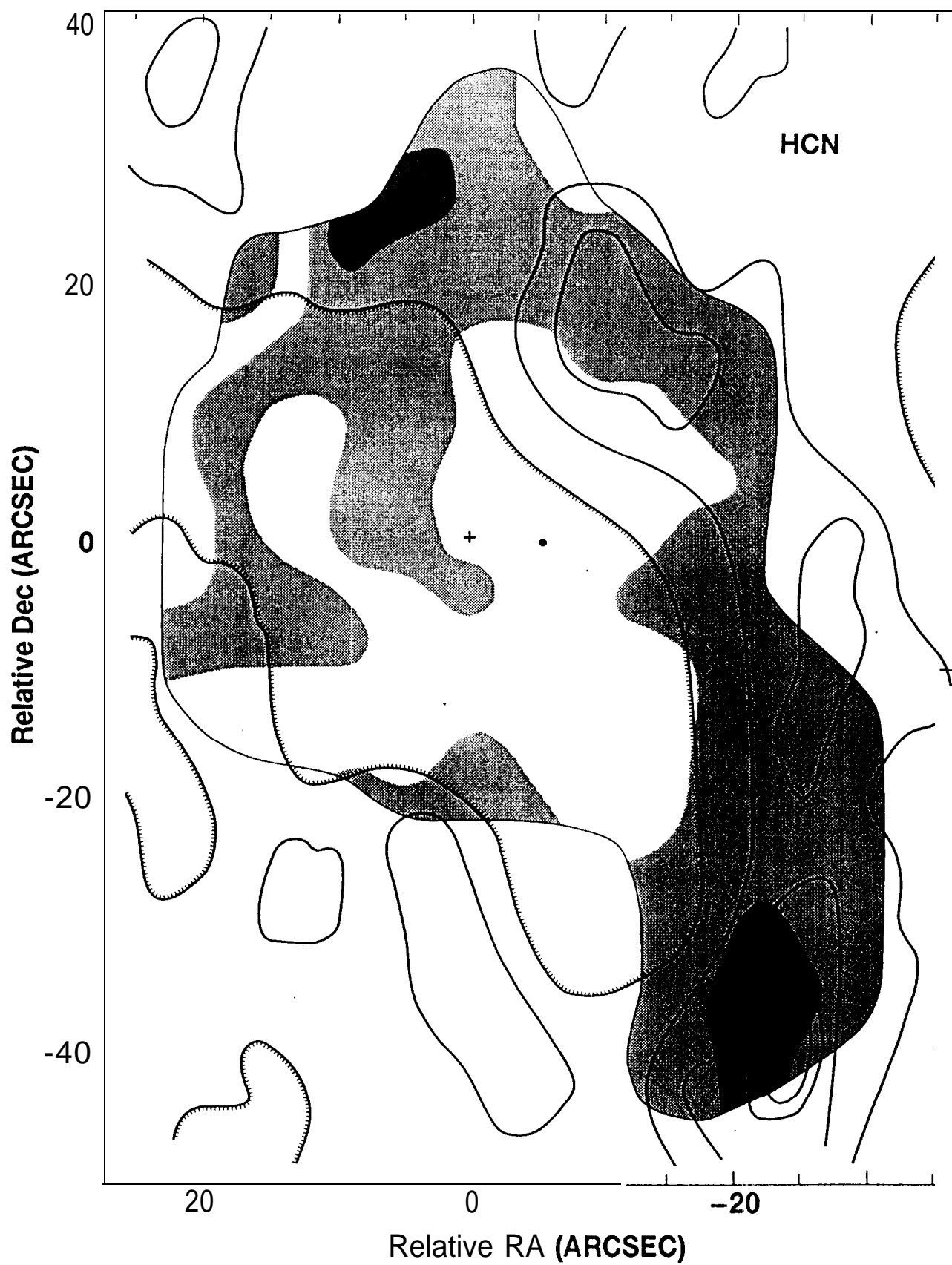


Fig. 6b

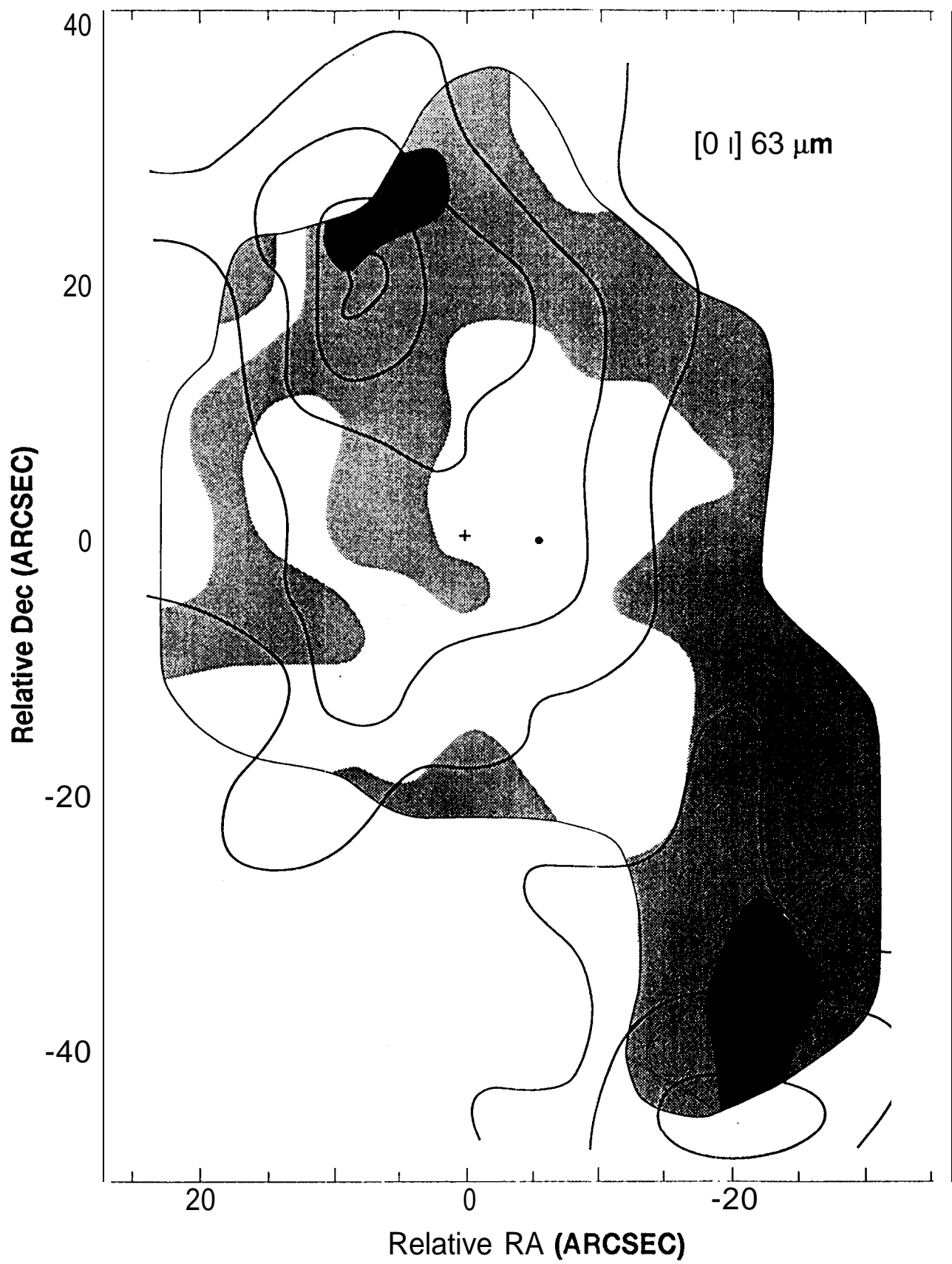


Fig. 6c

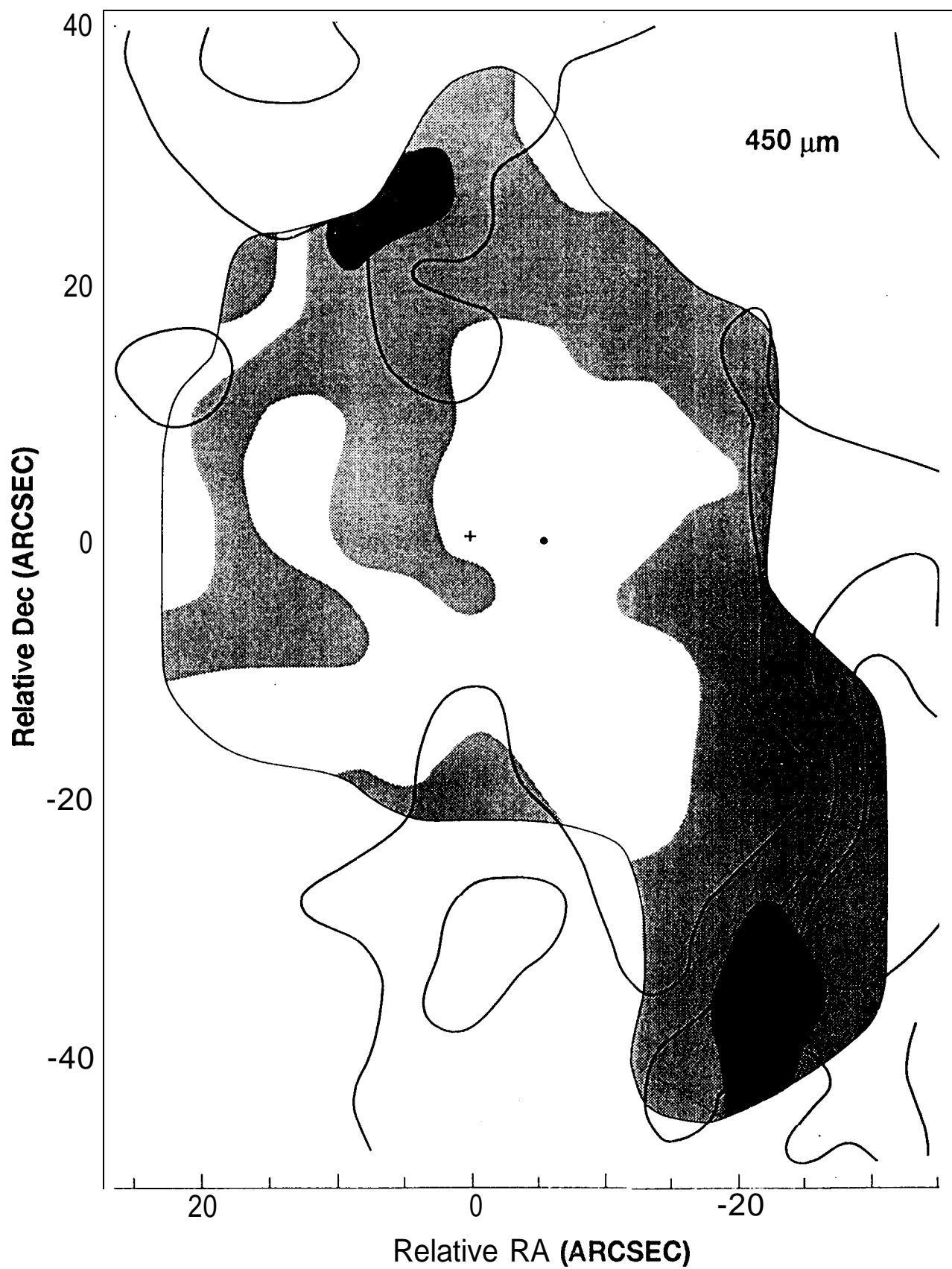


Fig. 6d

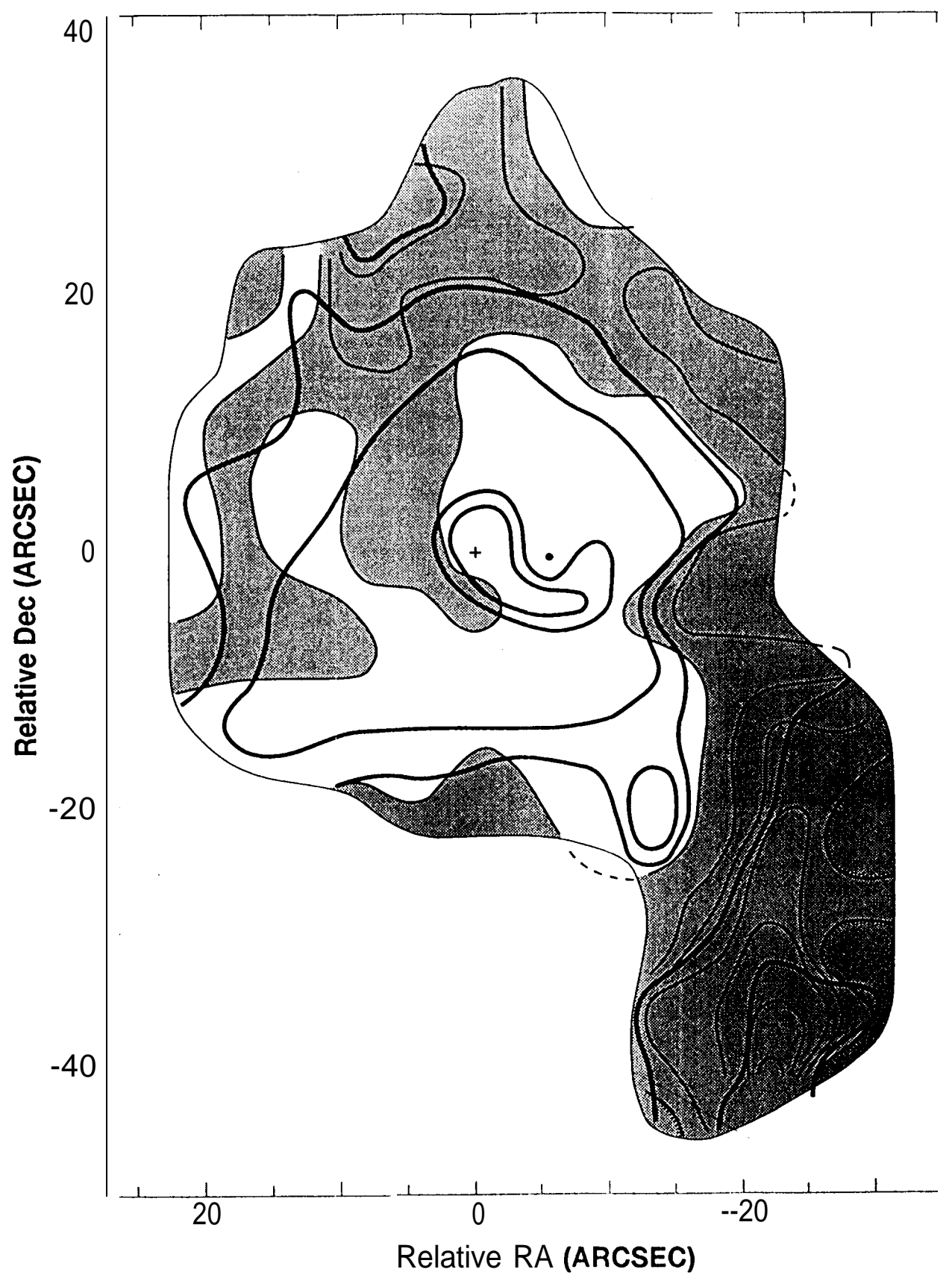


Fig. 7

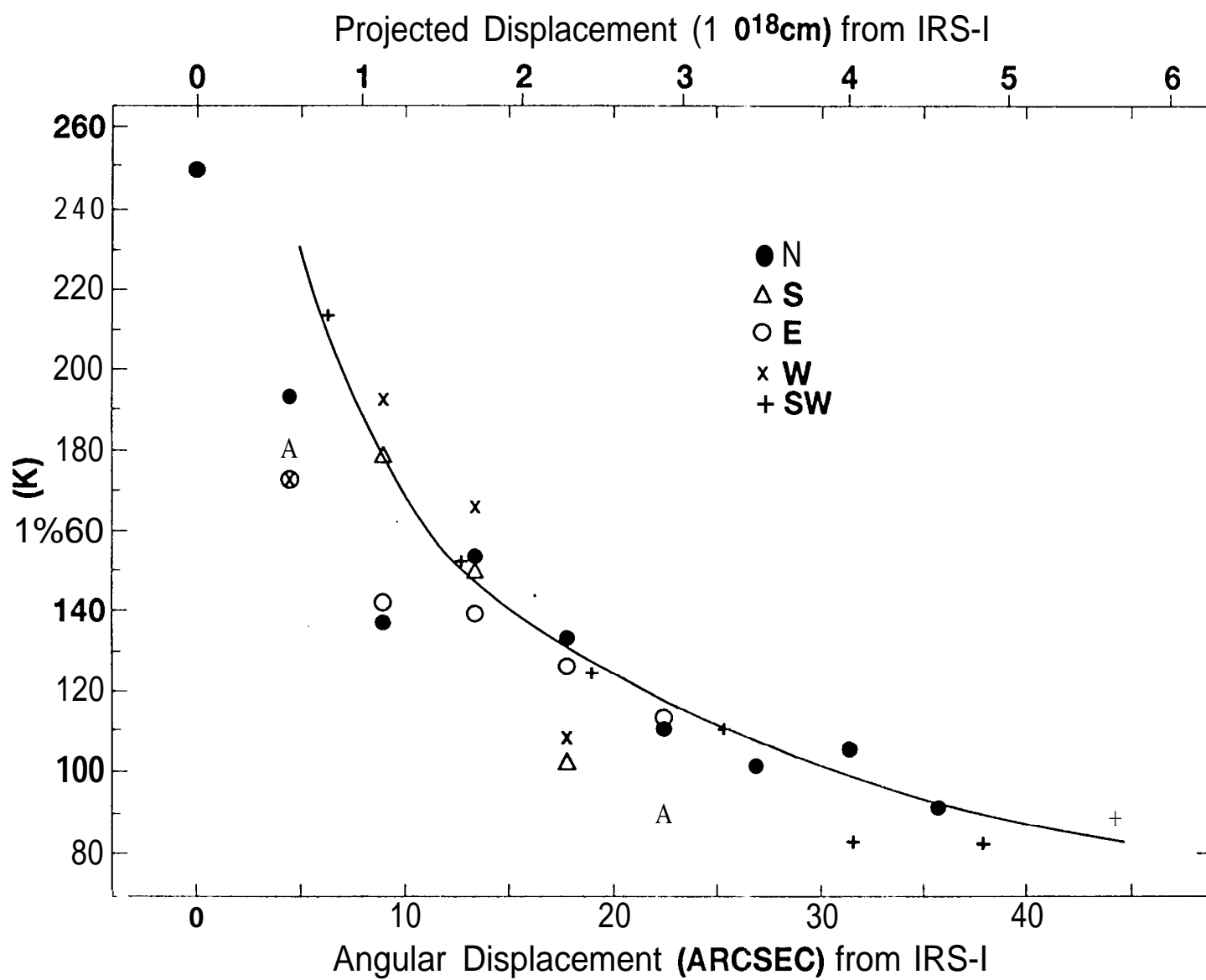


Fig. 8

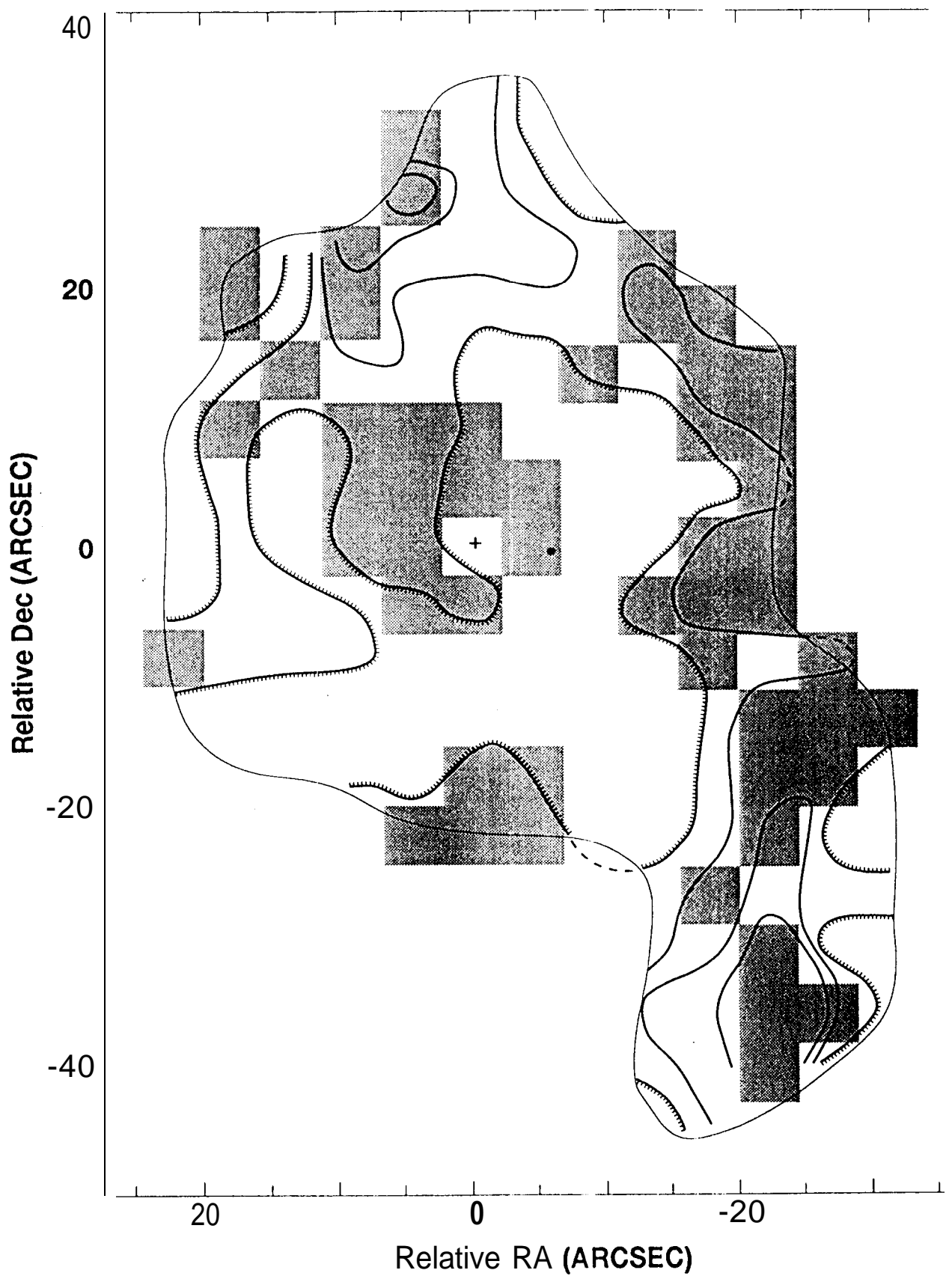


Fig. 9

